Naval Surface Warfare Center
Carderock Division

West Bethesda, Maryland 20817- 5700

Characterization of Regular Wave, Irregular Wave, and Large-Amplitude Wave Group Kinematics in an Experimental Basin

By

Lisa M. Minnick
Christopher C. Bassler
Scott Percival
Lauren W. Hanyok

20110719158

REPORT DOCUMENTATION PAGE

1. REPORT DATE *(DD/MM/YYYY)*	2. REPORT TYPE	3. DATES COVERED *(From - To)*
5-02-2011	Final	1-Aug-2009 – 31-Dec-2010

4. TITLE AND SUBTITLE	
Characterization of Regular Wave, Irregular Wave, and Large-Amplitude Wave Group Kinematics in an Experimental Basin	5a. CONTRACT NUMBER
	5b. GRANT NUMBER
	5c. PROGRAM ELEMENT NUMBER 0603563N

6. AUTHOR(S)	
Lisa M. Minnick, Christopher C. Bassler, Scott Percival, and Lauren W. Hanyok	5d. PROJECT NUMBER
	5e. TASK NUMBER
	5f. WORK UNIT NUMBER 09-1-9112-113

7. PERFORMING ORGANIZATION NAME(S) AND ADDRESS(ES) AND ADDRESS(ES)	8. PERFORMING ORGANIZATION REPORT NUMBER
Naval Surface Warfare Center Carderock Division 9500 Macarthur Boulevard West Bethesda, MD 20817-5700	NSWCCD-50-TR-2011/012

9. SPONSORING / MONITORING AGENCY NAME(S) AND ADDRESS(ES)	10. SPONSOR/MONITOR'S ACRONYM(S)
James S. Webster Naval Sea Systems Command SEA 05D1 Washington Navy Yard Washington, DC 20376	NAVSEA 05D1
	11. SPONSOR/MONITOR'S REPORT NUMBER(S)

12. DISTRIBUTION / AVAILABILITY STATEMENT
Approved for public release; distribution is unlimited.

13. SUPPLEMENTARY NOTES

14. ABSTRACT

An experiment was performed to measure and characterize wave kinematics in the Maneuvering and Seakeeping (MASK) basin at the Naval Surface Warfare Center Carderock Division (NSWCCD). The experiment is part of an ongoing effort to improve predictions and measurements of ship motions in waves, including more accurate characterization of the near-field wave environment and its influence on ship motions. The primary objective of this experiment was to measure and characterize the wave kinematics of regular waves of varying steepness and scaled irregular seaways, including irregular waves with embedded wave groups. Measurements, including free-surface elevations and velocity field measurements under the free surface, are presented and discussed.

15. SUBJECT TERMS
Regular Waves, Irregular Waves, Wave Groups, Particle Image Velocimetry, Deterministic Model Testing, Extreme Waves, Rogue Waves, Dynamic Stability, Slamming

16. SECURITY CLASSIFICATION OF:			17. LIMITATION OF ABSTRACT	18. NUMBER OF PAGES	19a. NAME OF RESPONSIBLE PERSON Christopher C. Bassler
a. REPORT UNCLASSIFIED	b. ABSTRACT UNCLASSIFIED	c. THIS PAGE UNCLASSIFIED	UL	86	19b. TELEPHONE NUMBER *(include area code)* (301) 227-5926

CONTENTS

FIGURES

Appendix A

Appendix C

TABLES

NOMENCLATURE

λ	wavelength
x	horizontal axis; positive in the direction of wave propagation
z	depth, calm water free surface at z=0, positive above the free surface
$V_{reference}$	reference velocity, based on nominal specified wavelength
V_x	x velocity component
V_z	z velocity component
V_{Total}	total velocity (x and z components)
H	wave height
H/λ	wave steepness
η	free surface elevation
η_0	wave amplitude
k	wave number; $k=2\pi/\lambda$
g	gravity
c	wave celerity
θ	wave phase angle
h	water depth
Hs	significant wave height
Tm	modal period
ω	wave frequency
Δt	PIV time step between successive PIV images in an image pair
φ	relative error in velocity vector direction

This page intentionally left blank

ABSTRACT

An experiment was performed to measure and characterize wave kinematics in the Maneuvering and Seakeeping (MASK) basin at the Naval Surface Warfare Center Carderock Division (NSWCCD). The experiment is part of an ongoing effort to improve predictions and measurements of ship motions in waves, including more accurate characterization of the near-field wave environment and its influence on ship motions. The primary objective of this experiment was to measure and characterize the wave kinematics of regular waves of varying steepness and scaled irregular seaways, including irregular waves with embedded wave groups. Measurements, including free-surface elevations and velocity field measurements under the free surface, are presented and discussed.

ADMINISTRATIVE INFORMATION

ACKNOWLEDGEMENTS

This page intentionally left blank

BACKGROUND

The largest waves and wave groups in a seaway represent the most challenging environmental conditions for a surface ship. These severe wave conditions must be considered for the assessment of ship performance, including seakeeping, dynamic stability, slamming and secondary loads, and ultimate structural strength. Severe stability events, or even capsizing, may result from several initial rare events, including single unusually high, steep, and possibly breaking waves, as well as sequences, or groups, of large waves which expose a ship to dangerous conditions.

Although not as well documented as single large wave events, eye-witness accounts have been made of ships experiencing wave groups, typically consisting of three large waves (Schuman, 1980; Buckley, 1983, 2005; Smith, 2006). These large-amplitude wave groups are often formed in developing seaways or by intersecting storms (Buckley, 1983; Toffoli, et al., 2004; Onorato, et al., 2006). The maritime accident investigation of the *Norwegian Dawn* indicated that the vessel had encountered three large waves in succession (NTSB, 2005; Broad, 2006).

A statistical comparison between regular wave groups and large-amplitude wave groups showed the largest wave is typically accompanied by two or three large waves and the probability of the largest wave occurring in a group is higher than for regular large waves (Goda, 1976). Additional characteristics of large-amplitude wave groups include the group period being longer than for regular wave groups. The narrowing of the spectral bandwidth for a seaway results in an increase in wave groupiness (Su, et al. 1982; Su, 1986; Yu and Liu, 1990). This spectral narrowing often occurs in a fetch-limited growing sea (Longuet-Higgins, 1976), where large-amplitude wave groups would most likely occur.

Su (1986) suggested a wave group with one or more extremely large waves would provide a better environmental design scenario than a single extreme wave or a regular wave group. Philips (1994) also expressed the need to develop a spatially-temporally defined extreme wave group for ship design. To predict rare response events, wave groups can present a scenario of higher probability for extreme response than a single large-amplitude wave. The "problem of rarity" is encountered when the time between events is long compared to the wave period (Belenky, et al., 2008; 2010). For both experiments and simulations, deterministic groups of large-amplitude waves can be applied to overcome the problem of rarity by inducing realistic severe conditions for large roll motions, stability failure, or structural failure at a known time and location (Bassler, et al., 2008; 2009; 2010; 2010a).

Tools have been developed for ship design where wave groups are used to induce a specific ship motion response. This approach was discussed by Blocki (1980) and Tikka and Paulling (1990) to study parametric roll, using wave groups to induce parametric excitation. Additional studies of the applications of wave groups to parametric roll response have been made by Boukhanovsky and Degtyarev (1996) and Spyrou (2004). Alford has used a design wave train method to produce a desired motion response (Alford, et al., 2006, 2007; Alford, 2008). Themelis and Spyrou (2007, 2008) deterministically predicted the required critical wave groups to induce instability for a ship. Then the probability of encountering one of these critical wave groups was

computed for a given route and duration. Using this critical wave group method, instabilities were assessed including synchronous and parametric resonance, as well as pure loss of stability. A technique to identify "worst sea" and "best sea" conditions for an offshore floating structure was applied by Fernandes, et al. (2008). This technique used both envelope and autocorrelation function approaches to determine the highest and smallest wave groups from a spectrum.

However, theoretical and numerical models to assess surface ship dynamic stability and secondary loads performance, specifically in severe seas, are not yet fully mature. For the near future, model experiments may continue to be the primary method to evaluate surface ship dynamic stability and secondary loads in severe waves. However, once simulation tools are fully developed, model experiments will remain a necessary method to Verify and Validate (V&V) numerical predictions (AIAA, 1998). An important consideration for validation is the accuracy of comparison between the numerical and experimental realizations of these rare events.

Model experiments to assess dynamic stability and secondary loads (slamming) performance are currently performed using two methods, testing in regular waves or irregular waves. Regular waves, often with wave length close to ship length, are commonly used to provide an initial assessment of ship response in critical wave conditions, for a range of wave steepness. Regular waves are easier to produce experimentally and can also be used to compare directly to simulation results. However, regular waves are not a realistic representation of the operating environment for a ship, and may also result in an overly conservative assessment of stability and structural performance. Irregular wave testing can be difficult because very long run times are needed to ensure extreme events with low probability of occurrence are realized, including large waves or wave groups. Because of the temporal and spatial limitations of the basin, it is impractical to ensure the extreme events are realized. In addition, due to their random nature, ship response in irregular wave conditions is difficult to compare between experiment and simulation, or even between realizations.

The first approach to reduce the number of required tests for regular wave seakeeping was the transient wave technique, developed analytically by Davis and Zarnick (1964). At the David Taylor Model Basin, Davis and Zarnick, and Gersten and Johnson (1969) applied the transient wave technique to regular wave model experiments for heave and pitch, at zero forward speed. These tests demonstrated a potential reduction by an order of magnitude of the total necessary testing time. The transient wave technique was also applied to model testing in Japan in the mid-1970s (Takezawa and Takekawa, 1976; Takezawa and Hirayama, 1976).

Clauss and Bergmann (1986), Clauss and Kuchnlein (1994, 1995), and Matos, et al. (2005) used a transient wave technique with Gaussian wave-packets to excite model ships and offshore structures in an experimental basin. Further revisions to this technique included using nonlinear transient wave trains and modified wave celerity to generate extreme waves (Clauss, 1999). Transient waves have even been proposed for use as part of a wave-maker calibration procedure (Masterton and Swan, 2008). Model tests have been performed with large transient waves, embedded in both regular and random wave trains. These waves were calculated both linearly and nonlinearly, with empirically-based terms for the particle orbital motion and shallow-water effects (Clauss and Hennig,

2002). Experimentally, single extreme waves have been shown to have larger asymmetry than full-scale storm waves, but with a profile more similar to real extreme waves than second-order numerical simulations (Antao and Guedes Soares, 2008).

To generate desired deterministic wave sequences in the experimental basin, techniques where singular extreme waves were embedded in irregular seas with a linear wave theory "first approach," and then optimized using a fully nonlinear approach have been investigated (Clauss, 2000; Clauss, 2002a; Clauss and Schmittner, 2005). Experiments using a modified "New Year Wave" have been conducted to assess both motions and structural response for floating offshore structures (Clauss, et al., 2008). Model tests, to induce extreme roll and capsize for a ship, must consider wave characteristics such as wave height and steepness, wave groupiness, and the velocity and direction of wave propagation (Clauss and Hennig, 2004).

"Numerical wave tanks" have also been developed for the deterministic analysis of ocean structure behavior in simulated single extreme waves (Clauss, et al., 2005; Ning, et al., 2008). Schmittner, et al. (2010) used a numerical wave tank to predict wave time traces measured in a wave basin. One numerical tank applies potential flow codes for fast computations and RANS codes to model breaking waves and fluid-structure interaction (Clauss, et al., 2005). Some agreement exists between computations and experiments, with potential flow and RANS used either separately, or coupled. However, wave heights are shown to be generally over-predicted in a numerical wave tank. Extreme waves simulated in numerical tanks have also been applied to predict structural loading on ships (Guedes Soares, et al., 2008) and offshore structures (Clauss, 2002b). However, loads predictions have been shown to vary widely, depending on the wave kinematics model employed for the evaluation (Selavounos, 2005; Stansberg, et al., 2008), models considered included second-order (Bitner-Gregersen and Hagen, 2004), Grue's method (Grue, et al., 2003), or the well-known Wheeler stretching method (Wheeler, 1969). Some comparisons between numerical predictions and extreme wave model experiments were also performed by Hennig, et al. (2006).

Improved understanding of the wave kinematics of large steep waves is also essential to the ship stability problem. Comparisons between the wave environment in numerical predictions and experimental and full-scale measurements are often made using only wave elevations. Because of the sensitivity of the ship response to the wave kinematics model used in numerical simulations it is important to determine the accuracy of the various wave models commonly employed. Particularly for panel-based methods, an accurate representation of the velocity field, and subsequent pressure field, below the free surface, is essential to characterizing the ship motion response correctly.

Several approaches have been undertaken to improve the numerical modeling of wave kinematics (Fenton, 1985). The velocity field for a deep-water Stokes wave was obtained numerically by Longuet-Higgins (2008). A fully-nonlinear three-dimensional method differentiating the surface displacement was used to calculate the horizontal orbital velocities of the measured moderate amplitude waves (Grue, et al., 2008). Some comparisons between wave kinematics numerical predictions and experimental measurements were also made by Graw (1994), Stansberg, et al. (1996), Grue and Jensen (2006), Hennig, et al. (2006), and Clauss (2008). Skjelbreia et al., (1989, 1991) performed an extensive series of laboratory experiments to measure regular and irregular

wave kinematics using Laser Doppler Veloeimetry (LDV). Partiele Image Veloeity (PIV) techniques have also been used to measure wave-field kinematics. Grue, et al. (2003), measured the veloeity profiles of 62 steep wave events and Choi (2005) used both LDV and PIV to measure the wave veloeities of regular, irregular, and extreme waves. PIV has also been used to mcasure both the veloeities and aeeelerations of wave events (Grue and Jensen, 2006; Jensen, et al., 2001; Jensen and Pedersen, 2004). Kristiansen et al (2005) explored the ability to use PIV as a tool for validation and verification of numerieal wave kinematies.

Swan, et al. (2002) detcrmined that empirieal eorrections for the fluid partiele kinematies in a linear random wave model did not accurately predict experimentally measured nonlinear wave loads on eylindrieal structures piereing the free surface. This result demonstrated the influence and sensitivity of the fluid particle kincmatics model for predieting nonlinear wave loads.

Given these eonsiderations, this technieal report details an experiment and subsequent analysis performed in FY09 and FY10, as part of a continued effort at NSWCCD to improve predictions and measurement of ship motions in waves and assess the dynamic stability and seakeeping performance of naval ships. Model experiments, such as the one deseribed in this report are neeessary to inerease understanding of the prineipal physics governing dynamie stability events, and to provide validation data for the development of simulation tools. This cxperiment employed particle image veloeimetry (PIV) techniques to obtain a data set of the vector field below the free surfaee for regular waves of varying steepness and realizations of irregular seaways both with and without embedded wave groups of large amplitude. This data will be used to provide additional physieal insight and validation data for wave kinematies models of moderate and steep regular waves, and irregular waves, including realizations of irregular seaways with large-amplitude wave groups.

EXPERIMENTAL APPROACH

Facility Description

This experiment was eondueted in the Maneuvering and Seakeeping (MASK) basin at NSWCCD (Figure 1). Eight pneumatic wave-maker units are located along the 73m (240 ft) west side of the basin and thirteen units along the 110m (360 ft) north side of the basin. The basin is 6m (20 ft) deep. A 115m (376 ft) bridge traverses the basin and ean be moved up to a 45-degree offset from the longitudinal eenter of the basin. The two perpendieular banks of wave-makers ean be operated individually to produee long-crested waves, or simultaneously to generate a bi-direetional wave-field. Sloping, perforated, conerete beaehes are loeated on each side of the basin opposite the wave-makers to minimize wave reflections.

Two methods are used to control the flow of energy into the wave-field: varying blower motor speeds supplying air to the pneumatie domes and varying the motion amplitude of the flapper valve that controls the air pumped in and out of the domes. Hydraulic cylinders with a ±10V control signal are employed to aetuate the flapper valves. The control signal is generated using a computer system and the digitized voltage signal is filtered with a low-pass smoothing filter and a high-pass eutoff frequency prior

to input to the wave-maker. The wave-maker also has a series of lips on each of the pneumatic domes, which can be set in a position of either up or down, to modify high frequency disturbances in the generated wave-field.

For these experiments, the MASK bridge was located in the middle of the basin, parallel to the north bank of wave-makers. In this configuration, the locations of the sonic probes are given in Table 1, measured from the south-west corner of the basin.
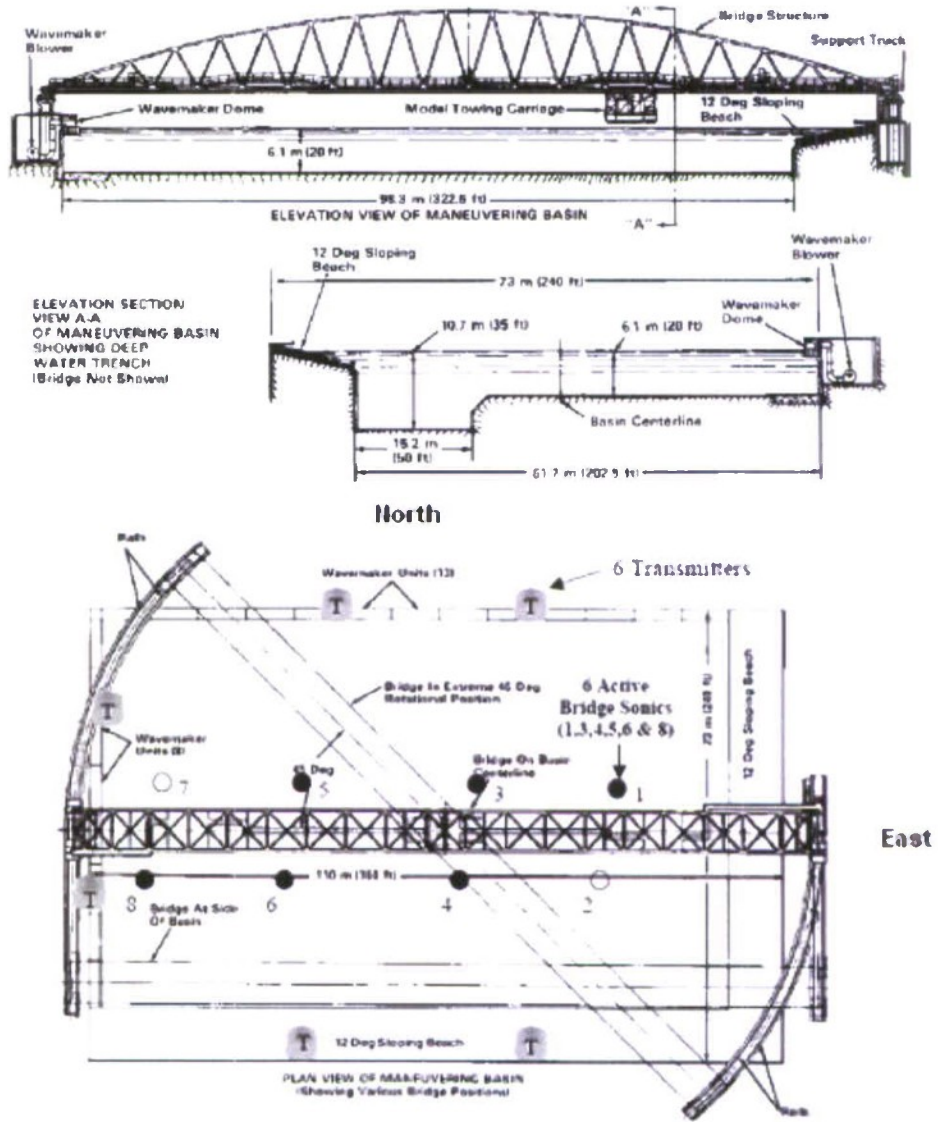
Figure 1. Schematic of the MASK basin with bridge mounted wave probes.

Table 1. Location of waveheight probes, measured from southwest corner of the basin.

Gage Name	Location x (m)	Location y (m)
Bridge Wave Ht #8	17.72	29.57
Bridge Wave Ht #6	35.66	29.57
Bridge Wave Ht #5	39.86	39.59
Bridge Wave Ht #4	60.07	29.57
Bridge Wave Ht #3	63.88	39.59
Bridge Wave Ht #1	90.62	39.59

Test Description

The primary objectives of this experiment were to: (1) characterize the kinematics of regular waves by examining the influence of wave steepness on the velocity profile and (2) characterize the kinematics of irregular waves with embedded wave groups by examining the effect of the wave group composition, location, and scaling. Secondary objectives were to: (1) identify the influence of the embedded wave groups on the generated spectral shape, (2) provide comparisons of wave height measurements obtained from the ultrasonic wave height probes and PIV images, and (3) provide a validation data set for wave theory and numerical simulation tool development.

Regular waves with steepness of 1/50, 1/30, and 1/15 and a constant wavelength of 4.81m were examined. Wave steepness 1/30 was tested previously with the ONR Topside Series hull form (DTMB Model 5613, 32nd-scale), as reported in Bishop, et al. (2005). The 1/50 wave steepness tested in this experiment was near the 1/60 tested in Bishop, et al. (2005). The third regular wave steepness (1/15) corresponds to the steepest regular wave that typically can be consistently generated using the MASK basin pneumatic wave-makers and also can be measured by the Senix probes without frequent measurement drop-outs. Regular waves were used to examine the influence of wave steepness on the velocity field below the free surface, and to provide comparisons between moderate to steep regular waves and a large-amplitude wave group in an irregular seaway.

Irregular wave conditions included 30th and 46th scale realizations of Hurricane Camille and a 30th scale Bretschneider Sea State 8 (BS-SS8) spectra, and included realizations both with and without embedded wave groups. These irregular seas conditions were previously used (Bassler, et al., 2008) to examine the feasibility of producing deterministic large-amplitude wave groups in the MASK basin. The two scales considered in this study represent nominal scale ratios for ship model testing at NSWCCD to assess ship performance for seakeeping and dynamic stability, as well as structural loads. A summary of the irregular wave conditions including significant wave height and modal period is provided in Table 2.

Three different wave groups were embedded in the Hurricane Camille spectrum and are denoted as groups 42, 43, and 44. All three groups occur at the same location in the

8

wave train. The composition of wave groups 42 and 44 are the same, while 43 varies slightly. Wave group 44 is a scaled version of 43. Similarly, two different wave groups were embedded in the BS-SS8 spectrum and are denoted as 37 and 38. The composition of the wave groups is identical; however, wave group 37 occurs near the end of the wave train while wave group 38 occurs close to the middle.

Table 2. Summary of irregular wave with embedded group conditions.

Condition	Hs inches	Hs mm	Tm sec
Camille 30th Scale			
Camille 30th-42	16	406.4	2.45
Camille 30th-43	16	406.4	2.45
Camille 46th Scale			
Camille 46th-44	10.3	261.6	1.96
BS-SS8			
BS-37	15	381	3
BS-38	15	381	3

Wave Generation Method

The conditions summarized in Table 2 consist of deterministic irregular waves with large amplitude wave groups embedded in seaway realizations. These conditions were generated following the previous method of Bassler, et al. (2008; 2009). In this method serial superposition is utilized to combine wave trains of variable periods, amplitudes, and cycles into larger or smaller amplitude waves, by either constructive or destructive interference.

The underlying principles of this method are the deep-water dispersion relation and phase velocity, which dictate that longer waves propagate faster than shorter ones. At the upstream position, a series of waves with varied amplitude and periods are generated by a wave-maker. As wave components propagate downstream, lower frequency components coalesce with the higher frequency components and increasingly larger waves are formed. The waves coalesce at a desired, repeatable location in the basin to produce a large group during a given wave realization. In general, larger waves can be produced with increased distance between the wave-maker and concentration position. The wave groups for this experiment were generated using four finite-wave sequences resulting in a three-wave group occurring at a single location in the MASK basin. The composition of the group can be changed by varying the individual finite-wave amplitudes and periods.

Linear wave theory is applied to calculate the group velocity and regular wave groups were calculated to coalesce at a determined concentration position. The wave-maker controller sequence files for wave generation were determined using equations 1-6.

Start time for *n*th regular wave train: $t_n = t_0 + \dfrac{T_n}{4} - T_n(Cyc_n - 1)$ (1)

Hydraulic cylinder voltage for *n*th wave train at time *t*:

$$V(t) = H_n \cos\left[\frac{2\pi\left(t - t_n - \frac{T_n}{4}\right)}{T_n}\right] \quad (2)$$

Time for the nth regular wave to reach test point: $t_p = \frac{x_a}{c_{Gn}} + \frac{T_n}{4}$ (3)

Deep-water group velocity of nth regular wave: $c_{Gn} = \frac{d\omega}{dk} = \frac{gT_n}{4\pi}$ (4)

Wavelength, $\lambda = \frac{g}{2\pi}T_n^2$ (5)

Wave steepness, $s = \frac{H}{\lambda}$ (6)

where T_n is the period of the nth regular wave in seconds, H_n is the voltage of the nth regular wave (amplitude of flap motion), Cyc_n is the number of cycles of the nth regular wave, x_a is the distance to the concentration location (in meters), and t_0 is the zero time before waves start in seconds. Local g is $9.80100 \text{ m/s}^2 \pm 0.0004$.

Experimental Set-Up

The MASK bridge was positioned in the middle of the basin, parallel to the long bank, and the carriage was positioned at the midpoint of the bridge. The waves were generated from the short bank, on the west side of the basin (Figure 1). Wave data was collected from the six ultrasonic wave probes mounted from the bridge (Figure 1) and the measurement plane was positioned near ultrasonic probe 3. At the probe 3 location, with the bridge in the center position, the wave-field is expected to be unidirectional. Effects from the basin wall were shown in numerical prediction using WAMIT (O'Dea and Newman, 2007) to result in slight curvature on the north and south ends of the wave front (Figure 1). However, in the center of the basin, the effects from the basin walls and curvature of the wave-field should be minimal (Smith, et al., 2007) and thus able to be neglected, and the wave-field appropriately considered unidirectional. Although not directly measured, the experimental observations appear to confirm that the waves in the region of the basin may be assumed unidirectional and practically uniform.

A schematic of the experimental set-up is shown in Figure 2. The PIV camera system was mounted to the carriage in the MASK basin. Waves were generated from the short-bank wave-makers and propagated from west to east (Figure 1). A 0.9m by 0.9m (3 ft by 3 ft) field-of-view for PIV measurements, oriented east-west and vertical, enabled a two-dimensional cut of the waves in the direction of wave propagation.

The PIV camera was mounted 2.86m (9.4 ft) south of the measurement plane, with a look-up angle of 10 degrees. The camera field-of-view was split with 0.409m (16 inches) above and 0.486m (19 inches) below the calm water free surface. The camera was submerged in the basin, using a waterproof housing and attached to a strut system mounted on the MASK carriage. The center of the PIV measurement field of view was

located 0.0254m (1 inch) east and 0.64m (25.25 inches) south of ultrasonic wave probe 3 (Figure 1, Table 1).

To illuminate the PIV measurement plane, two waterproof laser probes were attached to a submerged tripod and oriented to produce a 19mm (0.75 inch) thick vertical light sheet parallel to the direction of wave propagation. The lasers were located on the carriage and the laser beams were channeled into fiber optic cables connected to the submerged laser probes. Each laser probe is comprised of a 0.3m (12 inch) long cylindrical housing which contains a series of optical lens designed to expand and spread the beam into a light sheet.

The PIV measurement field was seeded with small silver coated particles, nominally neutrally buoyant and 100µm in diameter using a mechanism attached to the MASK carriage. The mechanism consisted of a 50.8mm (2 inch) diameter PVC pipe, closed at one end, with the other end connected by a hose to a pump in a particle mixing tank on the MASK basin carriage. A series of perforations were drilled along the vertical length of PVC pipe east to west, in the direction of wave propagation.

For each measurement condition, particles were mixed with water in a mixing tank and pumped through the hose to the seeding mechanism. The mix was a compromise between low density (for uniform particle dispersion) and high density (to minimize the flow rate and subsequently the induced velocities into the measurement region of the flow). The PVC pipe was lowered into the water and manually traversed along a beam adjacent to the carriage, dispersing particles into a region parallel to the direction of wave propagation. After the desired particle concentration was achieved, the PVC pipe was raised out of the water to remove it from the flow field.

For each experimental condition, the following procedure was carried out. After seeding, the pneumatic wave-maker was increased to the required blower rpm and the specified wave voltage signal was input to the wave-maker control. The wave-maker then began to produce waves and data collection began.
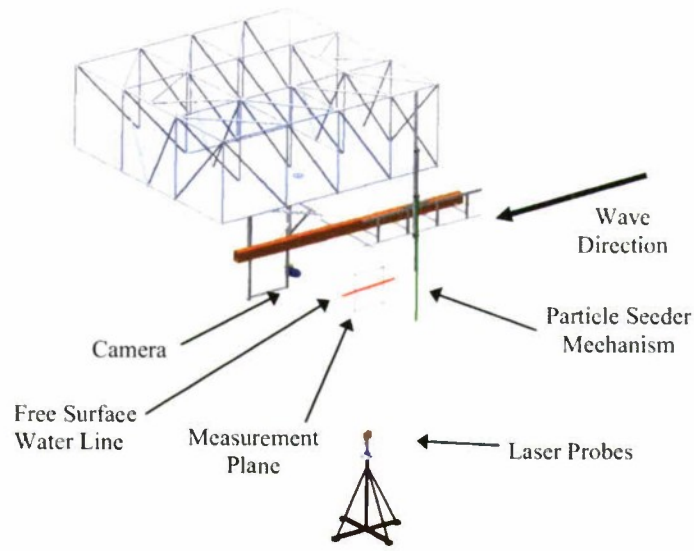
Figure 2. Illustration of the experimental set-up in the MASK basin, including PIV instrumentation and seeding mechanism.

Wave-Maker Operation

To generate unidirectional long crested waves, individual wave-maker units in each bank were operated in-phase and produced wave segments of the same nominal amplitude. Wave periods for each individual wave-maker unit can be either regular or random. For this test, waves were generated from the short bank wave-makers on the left side and travel from west to east across the basin, as shown in Figure 1.

Regular Waves

To generate regular waves in the MASK basin, the wave-maker control uses a combination of parameters to achieve the desired amplitude and wave period. These parameters are the pneumatic blower (rpm) and a wave frequency (Hz). The parameters used for this experiment are given in Table 3. The blower (rpm) values correspond to 1/50, 1/30, and 1/15 wave steepness, respectively. The wave frequency corresponds to a wave length of 4.81m. This wave length was chosen based on the ship length for DTMB Model #5613-1 (Bishop, et al. 2005), a notional naval combatant hull form, which has been used for numerous subsequent research model experiments.

Table 3. Wave-maker parameters for regular waves.

Parameter	Value
Blower (rpm)	600, 900, 1500
Frequeney (Hz)	0.570

To generate regular waves the wave-maker control program employed a sequence file of voltages programmed at 40 cycles per second. The computer generated digital control voltage sequences are created with a digital-to-analog (D/A) converter. The digitized voltage signal is filtered with a low-pass smoothing filter and a high-pass cutoff frequency prior to input to the wave-maker.

In this study, a sequence file is a sinusoidal wave converted to a voltage signal for the hydraulic wave-maker piston. The regular waves were controlled by blower rpm, maximum voltage (the amplitude of flapper motion), frequency, and the number of wave cycles.

Irregular Waves

A computer program was used to generate irregular waves. The program produced digital control signal sequences and supplied them to the wave-maker controller through a digital-to-analog (D/A) converter. The digital control sequence software uses a filtered white noise technique, with 30 random seeds and is produced using a 40 Hz sampling rate for the wave-maker control signal. To produce a desired wave spectrum, a computer generated white noise signal was used to actuate the flapper valves, resulting in wave-maker dome pressure fluctuations. The wave energy distribution, as a function of the frequency, was adjusted with the driving frequencies for the valve controls. The blower speed was adjusted to control the wave amplitude.

To represent nominal conditions for extreme waves, two long-crested irregular wave spectra were considered for this study, a 30th scale Bretschneider wave spectrum for Sea State 8 and both 30th and 46.6th scale Hurricane Camille wave spectra.

Irregular Waves with Embedded Groups

Wave sequences generated for particular pneumatic wave-maker blower rpm, signal amplitudes, and frequencies (Table 3) were applied to generate wave trains designed for the desired group structure, with repeatable wave properties, at a fixed location within the MASK. The finalized sequence file was a summation of the voltages for the four wave trains. In some sequences, a flat spot existed, due to the signal frequency interaction, and was removed manually to smooth the motion of the hydraulic pistons. Each deterministic embedded wave group consisted of three large-amplitude waves.

INSTRUMENTATION

Measurements of the spatial velocity field at a specified location in the basin, the free surface at multiple locations in the basin, and video were collected during this experiment.

Velocity Field Measurements

Particle Image Velocimetry (PIV) was used to obtain velocity field measurements beneath the free surface of the waves. PIV is an optical, non-intrusive, flow-field measurement that provides in-plane velocity measurements of a planar cross-section of a flow. Neutrally buoyant particles are used as flow tracers to provide an indirect velocity measurement. The tracer particles are illuminated twice in a small time period by two consecutive laser pulses. The light scattered by the particles is recorded by a high speed

13

charge-coupled device (CCD) camera. The distance traveled by the tracer particles in the measurement region, as observed by the recorded images between laser pulses, is used to obtain the displacement and velocities throughout the measurement region.

For evaluation, each image is divided into small interrogation regions and analyzed as image pairs (Figure 3). An image pair is defined as two images recorded within a small time step between laser pulses. Corresponding interrogation regions between images in a pair are compared and the displacement of the tracer particles in these regions between images is determined using a cross-correlation function. The signal peak of the correlation function identifies the particle displacement for a given interrogation region. The velocity vector field is then calculated over the entire measurement field using the determined particle displacement and time between images, resulting in one velocity vector for each interrogation region.

Interrogation Windows

Image A

t

Image B

t + Δt

displacement
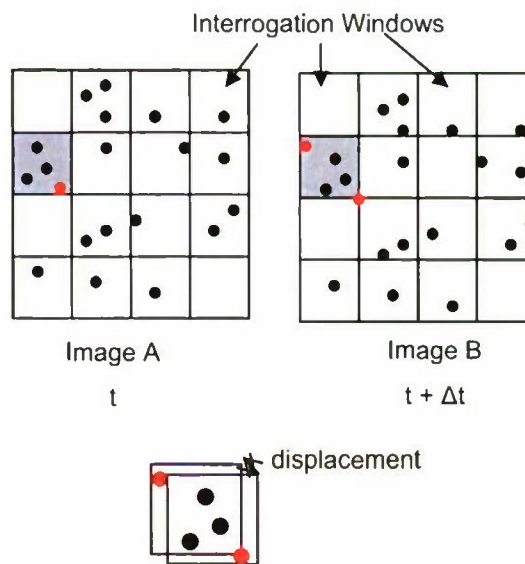
Figure 3. Schematic of interrogation windows and PIV evaluation method.

Camera

A MegaPlus ES 4.0/E camera was used to capture the PIV images. The camera has a spatial resolution of 2048 pixels x 2048 pixels and was operated in dual exposure mode at a frame rate of 10 fps. An image pair was taken every 200ms resulting in 5 image pairs per second. The camera was fitted with a 35 mm lens and stopped down to an f-number of 4.0 to provide the necessary depth of field. The time between images in a pair (Δt) was varied based on the flow characteristics for the condition being measured. The highest accuracy is obtained by maximizing the particle displacement within the interrogation region. For this experiment, the Δt between successive pulses varied from 1-30 ms, depending on the wave condition.

Lasers

Two custom built *Cynosure* flashlamp-pumped dye lasers operating at 585 and 595 nm were used to create a laser sheet, nominally 19mm (3/4 inch) thick, to illuminate the

flow field. The lasers were operated at a maximum optical energy output of 1 J/pulse and the laser beam was coupled into 600 micron optical fibers, 30m in length. The ability to launch the beam into the fibers allowed for more flexibility in the experimental setup. When operating at full power, roughly 700mJ/pulse is recorded at the output end of the fiber.

PIV Data Acquisition

The PIV data acquisition system was built by Boulder Imaging, Inc. VisionNow software captured and stored the images at the full camera rate onto a real time disk array with the capacity of 480 GB. The collection of the PIV images was synchronized with the ultrasonic wave probe 3 and each image pair was time-stamped to ensure correlation with the wave surface elevation data.

Flow Tracer Particles

Silver-coated hollow glass spheres (Potters Industries product AGSL150-S16) with a mean size of 110 microns and a specific gravity of 0.9 ±0.3 were used as flow tracer particles in this experiment. Scattered light from the particles in the illuminated measurement region was recorded by the camera.

Wave Surface Elevation Measurements

Single point wave height measurements were collected from an array of six bridge-mounted wave probes (Figure 1) sampled at 40 Hz. Wave data collected from sonic probes on the bridge were recorded at 40 Hz. The *Senix* model ULTRA-SR-BP sonic sensor transmits a conical sonic beam with a nominal 12-degree total angle and measures the time of reflection from the target to calculate the distance. Measurements for steep waves may have drop-outs because the water surface tends to scatter the sonic beam away from the sensor. The probes were connected to a computer on the bridge that transmits the wave data to a shore computer, where the data are collected and stored. Zeroes were taken at the beginning of each testing session, typically twice a day, to obtain more accurate test data and to account for small changes in the water level of the basin.

Video

A digital video recorder was used to document individual runs during the experiment. Video was used to record the wave-field and visually document large-amplitude wave events. However, due to the lack of an explicit visual reference for the wave-field (ie. no ship model), the visual data is not included in the analysis and discussion of the experiment presented in this report.

INSTRUMENT CALIBRATION AND UNCERTAINTY

Senix Ultrasonic Wave Probes

The Senix wave gages were calibrated in-situ, by varying the distance above a measured calm water level in the MASK. The transducers were located via precision machined pin locations with an estimated uncertainty of ±0.127 mm (±0.005 inch). The calibration range was ±381 mm (±15 inches), in 127-mm (5-inch) increments. The

ealibration loeations were –381, -254, -127, 0, +127, +254, +381 mm (-15, -10, -5, 0, +5, +10, +15 inehes).

The analog output for the Senix is 0 to 10 V DC. Data from the Senix were eolleeted and proeessed on a PC. The data were digitized with a National Instruments 16-bit data aequisition eard, NI 6036, at a sample rate of 24 Hz. The anti-aliasing filters are Frequeney Deviees D78L8L, set at a eutoff frequeney of 8 Hz. Typieal data eolleetion time was at least 100 s.

Calibration and Uncertainty

The normal nominal gain setting for the Senix is 76.2 mm/V (3 inehes/V). The noise level of the Senix for measurements over ealm water is typieally between 1 and 10 mV. The maximum Type A expanded uneertainty from the ISO GUM (1995) is ±0.048 mm (±0.0019 ineh) for 1,000 samples, or 41.7 s averaging time. The Type A standard uneertainty is defined as

$$u_A = \frac{s_h}{\sqrt{n}} \tag{7}$$

where s_h is the standard deviation of the height and n is the number of samples. The expanded uneertainty is defined as

$$U = k_f u \tag{8}$$

where k_f is the eoverage faetor. Normally at the 95% eonfidenee level, $k_f = 1.959 \approx 2$. The maximum eombined and expanded uneertainty from these two elements is 0.135 mm (0.0053 ineh). The eontribution of the Senix noise is negligible, eompared to the machining aeeuracy of ±0.127 mm (±0.005 inch) for the positioning device.

An example calibration plot is presented in Figure 4, as a residual plot, for Senix wave gage #1. A residual plot is the differenee between the data and a linear regression fit. The dashed line in Figure 4 is the predietion limit at the 95% confidenee level, from the calibration theory of Seheffe (1973) and Carroll, et al. (1988). The uneertainty in the measurement from the instrument noise and position is smaller than the symbols in the figure. The red symbol in the figure is an outlier and was exeluded from the linear regression analysis.

The outlier is eaused by the over-ranging of the Senix, in this ease at 10 V. Due to the loeation of the Senix sensor relative to the water at 0 (zero) mm, the transdueer may over-range at either 0 or 10 V, but not both. In a few cases, the sensor was located relative to the water so that over-ranging did not oeeur.

Most of the ealibration uneertainty is due to the data seatter in the ealibration. The eontributions from instrument noise and position are quite small by eomparison. The relative uneertainty in the ealibration is presented in Figure 5. As Figure 5 indieates, the maximum relative uncertainty is about ±2%. The relative uneertainty is eomputed from the full-range (fr) value, whieh is nominally 381 mm (15 inehes).

Table 4 is a summary of the ealibration data aequired before the test. In this ease, the ealibration data were reported for the position of the probe above the water. In the experiment, the gage remained fixed, and the water moved relative to the gage. In the

16

data processing routine, the signs of the gain and slope were opposite those in the table. The slope is negative and the intercept positive for the wave measurements.

In Table 4, the column *SEE* is the standard error estimate from the linear regression analysis, while the *r* in the next column is the correlation coefficient. The *SEE* is essentially the standard deviation of the curve fit and is a measure of the randomness of the data. The precise definition may be found in most texts on statistical analysis, such as Ross (2004). For a highly linear curve fit, *r* is near one as indicated in the table, and *SEE* will be near zero.

The column *t-test*, is the result of a hypothesis test for a comparison of the measured slope to the nominal slope of 76.2 mm/V (3 inches/V) from Ross (2004). The column t_{95} is the value of the inverse Student-*t* from the hypothesis test. Any value from the *t-test* that is less than t_{95} is statistically the same as the nominal slope. From the table, the only wave gage that is different from the nominal slope is #6.

The last two columns are the expanded uncertainty of the gages at the 95% confidence level, at 10 Vdc. The last column is percent full-range (% fr) from the measured slope, where the nominal full-scale value is 381 mm (15 inches). As the table indicates, the largest uncertainty was about ±8 mm (±0.31 inches), or ±2% fr, at the 95% confidence level.

Because the calibrations are performed on a flat-plane surface, the accuracy associated with signal drop-outs when attempting to measure steep waves should be considered. However, the influence of wave steepness on signal drop-outs for the Senix probes is not currently known.
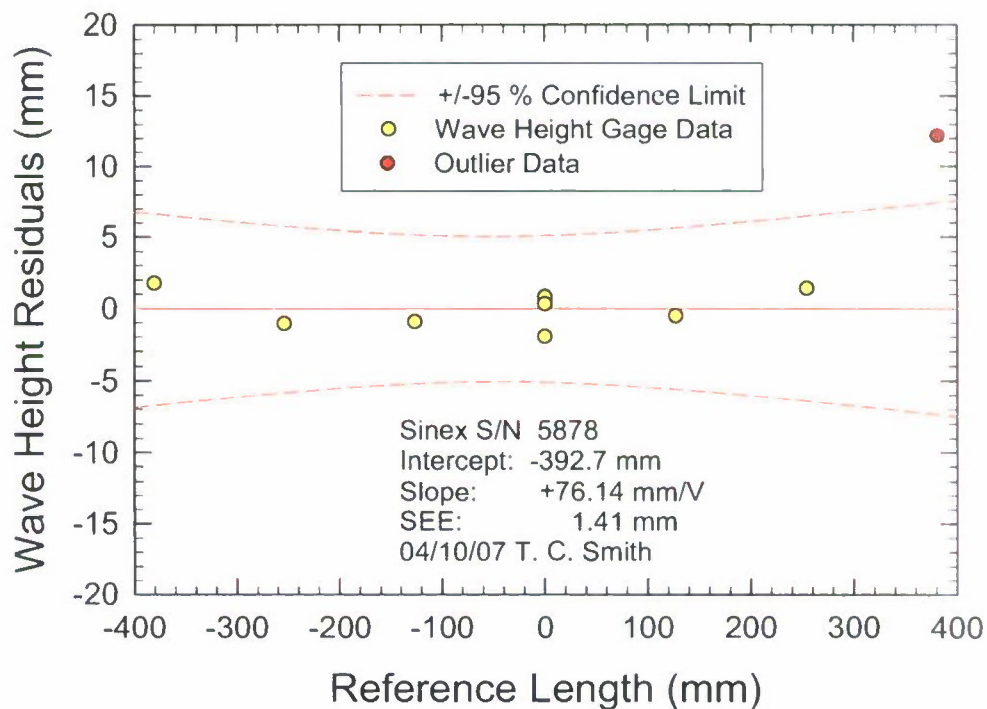
Figure 4. Calibration of Senix wave gage #1
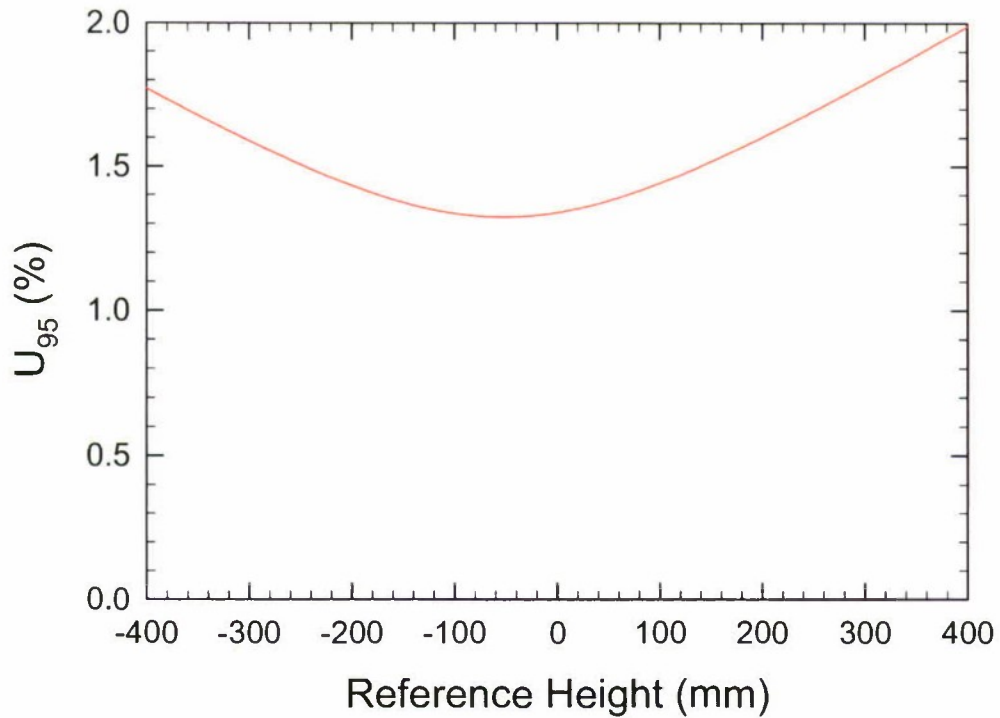
Figure 5. Relative calibration uncertainty of Senix wave gage #1

Table 4. Summary of Senix Wave Gage Calibrations

Probe #	Slope	Intercept	SEE	r	t-test	t_{95}	U_{95}	U_{95}
	(mm/V)	(mm)	(mm)				(mm)	(% fr)
1	76.138	-392.67	1.410	0.999979	0.308	2.45	7.33	1.93
3	76.325	-380.34	1.808	0.999975	0.611	2.36	7.99	2.09
4	76.269	-390.20	0.945	0.999991	0.515	2.45	4.92	1.29
5	76.314	-381.16	1.844	0.999977	0.545	2.45	8.50	2.23
6	76.538	-392.73	0.679	0.999995	3.51	2.45	3.53	0.92
8	76.313	-395.16	0.358	0.999999	2.24	2.45	1.85	0.49

Particle Image Velocimetry

Calibration

A spatial calibration of the PIV images was performed using *La Vision* DaVis software v7.2. A calibration target, 91.44 cm x 91.44 cm (36x36 inches) in size and machined to ±0.00254 cm (0.001 inch) accuracy, is shown in Figure 6A. The target contains 121 evenly spaced '+' marks, 50.8mm (2 inches) in height and width. The target was mounted in the MASK basin prior to the experiment coincident with the location of the measurement plane. For the experiment, 406 mm (16 inches) of the measurement plane was above the calm water free surface. To calibrate the images the target needed to be fully submerged therefore it was mounted 40.64 cm (16 inches) lower than then actual measurement plane so its top was even with the water surface. The camera was adjusted accordingly for calibration. The position of the laser probes were adjusted until the laser light sheet was visually aligned with the face of the calibration target. A calibration image was taken (Figure 6A) and imported into the DaVis software. The software creates a mapping function as well as applies a dewarping function to correct distortions due to the 10 degree look up angle of the camera. Figure 6B shows the dewarped image and the results of the mapping function, shown in red. The RMS of the fit was 0.12 pixels.
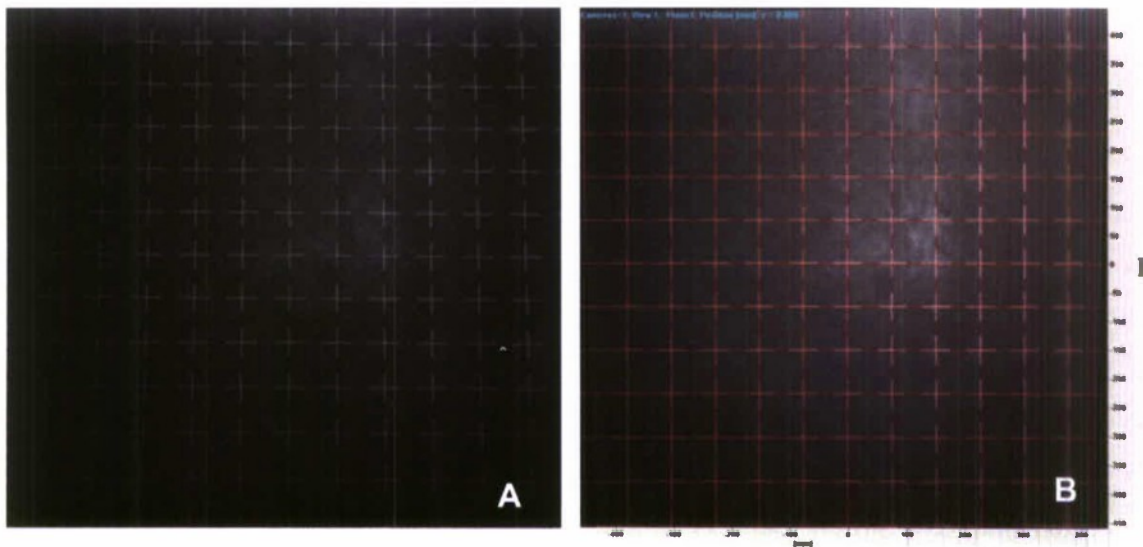
Figure 6. Calibration image (A) and dewarped image with mapping function (B) shown in red.

Uncertainty

Uncertainty analysis includes both an analysis of the accuracy and the repeatability of a measurement. The accuracy of the measurement, often referred to as the systematic or bias error, is typically a fixed or constant value. The repeatability of a measurement refers to the random variation in the measurement and typically includes factors the experimentalist has little to no control over. Specially, in terms of PIV uncertainty for this experiment, the calibration and experimental setup are classified as part of the bias error and an assessment of the repeatability includes variability in the wave-maker, the

precision in the determination of the PIV time steps, and the consistency of the PIV seeding. This section presents a method to quantify the repeatability of PIV measurements.

PIV images pairs were taken every 200ms. For the regular wave conditions one wave period traveled through the PIV measurement plane in approximately 1.76 sec and each processed image pair captured approximately 18.6% of the wavelength, with approximately 39% overlap between successive images. A comparison of the velocity measurements of the overlapping region between successive PIV images was used to provide information about the repeatability of the PIV measurements. Inherent in this repeatability is a measure of the repeatability of the generated waves.

For each regular wave condition, the overlap region between successive images was identified and the total velocity vectors were compared. The relative error in both the magnitude and direction (φ) of corresponding velocity vectors was calculated as shown below.

$$relative\_errror\_mag = \frac{\left| |V_n| - |V_{n+1}| \right|}{|V_n|} \tag{9}$$

$$relative\_errror\_direction = \phi = a\cos\left(\frac{V_{X_n} V_{X_{n+1}} + V_{Z_n} V_{Z_{n+1}}}{|V_n||V_{n+1}|} \right) \tag{10}$$

where:

$$\vec{V}_n = V_{X_n}\hat{i} + V_{Z_n}\hat{k} \quad \text{and} \quad |V_n| = \sqrt{V_{X_n}^2 + V_{Z_n}^2} \tag{11}$$

$$\vec{V}_{n+1} = V_{X_{n+1}}\hat{i} + V_{Z_{n+1}}\hat{k} \quad \text{and} \quad |V_{n+1}| = \sqrt{V_{X_{n+1}}^2 + V_{Z_{n+1}}^2} \tag{12}$$

$$V_n \cdot \vec{V}_{n+1} = V_{X_n} V_{X_{n+1}} + V_{Z_n} V_{Z_{n+1}} \quad \text{or} \quad V_n \cdot \vec{V}_{n+1} = |V_n||V_{n+1}|\cos(\phi) \tag{13}$$

Figure 7–Figure 12 provides plots of the relative error in velocity magnitude and velocity direction for regular wave cases 1/50, 1/30, and 1/15 respectively. Each colored strip in the plots represents a portion of the wave for which an overlap region exists. A total of 28 consecutive cycles were measured for each condition, however for visualization purposes only a portion of the overall run is shown in the plots. In addition, for visualization purposes the x-axis has been compressed. Further details regarding this presentation of the data may be found in the Results section.

A comparison of the relative error in velocity magnitude among conditions shows the relative error is smallest in the 1/30 waves. The 1/50 waves show the error is consistently greater for the wave troughs than the wave crests. This is likely due to the method used to choose the PIV time step. The time step was chosen so, at the maximum expected velocity, the tracer particles would be displaced 8-12 pixels from image A to image B within a given image pair. The maximum velocity was expected to occur just below the water surface therefore, the time step was optimized for those velocities. As a result, the precision of the measurement for velocities larger or smaller than this is reduced. This trend is most apparent in the 1/50 wave, but applies to the 1/30 and 1/15

waves as well. It is likely the smaller difference in error from crest to trough in the 1/30 waves suggests the chosen time step is less biased toward the crest velocities than for the 1/30 time step. In general, the repeatability in wave form for the 1/15 waves is poor, leading to a more random distribution of error. It is also important to note the quality and consistency of the seed distribution within each PIV frame is also likely to have an effect on the relative error. In general, the quality of the seed distribution decreased with increasing depth in the measurement plane. It is likely the large values of relative error present closer to the bottom of the measurement plane are due to this. Some error is also introduced because the wave changes with time. The wave is progressing therefore the overlap regions represent the same portion of the wavelength, but the wave itself is not exactly the same from one instant to the next.

A comparison of the relative error in direction shows the largest range in error is observed in the steepest waves (1/15), but overall there is less variability among conditions than observed for the velocity magnitude.

For each overlap region shown in Figure 7–Figure 12 an average relative error was calculated and then an overall average for the entire run was computed. These averages, as well as standard deviations and RMS values, are shown in Table 5. As seen in the plots, the smallest values are observed in the 1/30 waves. The difference between the RMS values and average error values provides an indication of the amount of scatter in the relative error throughout the run. The larger the difference between the average and RMS values, the greater the amount of scatter. This is also confirmed by the values of standard deviation. The large standard deviation for the 1/15 wave steepness is likely a result of the variability in the wave-maker rather than the PIV measurements. As discussed in the Results section, 1/15 wave steepness for the specified wavelength is near the limits of the MASK wave-maker and the repeatability from one wave to the next is not as consistent as for less steep conditions.

The information presented in Table 5 provides an insight into the repeatability of the PIV measurements. The ability of the wave-maker to produce a repeatable condition has not been removed from these values and accounts for some of the variation in error. As presented and discussed in the results section, the 1/30 wave steepness is shown consistently to be the most repeatable condition. This analysis is consistent with this conclusion.

It is still important to note these values are presented to provide some insight to the overall uncertainty in the PIV measurements, but a formal analysis has not been completed. Specifically, an analysis of the accuracy component of PIV uncertainty has not been completed. Typically, a control run is performed to help quantify the uncertainty in the experimental setup. For this experiment collecting data in calm water would have been an appropriate control run. For this case zero velocity should be seen across the measurement plane and the presence of any velocities would indicate the amount of uncertainty introduced by the experimental setup and seeding process. Unfortunately, data of this nature was not collected. However, it is not unreasonable to assume the accuracy component of the uncertainty is the same order of magnitude as the repeatability. Therefore a conservative estimate of the combined accuracy and repeatability of the measurements would double the values presented in this assessment.

Table 5. Summary of relative error, standard deviation, and RMS values.

Wave Steepness	Average Relative Error		Standard Deviation		RMS	
λ/h	Direction deg	Velocity %	Direction deg	Velocity %	Direction deg	Velocity %
1/50	3.02	5.17	2.2	4.10	3.73	6.62
1/30	2.37	3.95	1.8	3.10	2.95	5.05
1/15	2.82	5.06	2.3	8.90	3.62	7.08
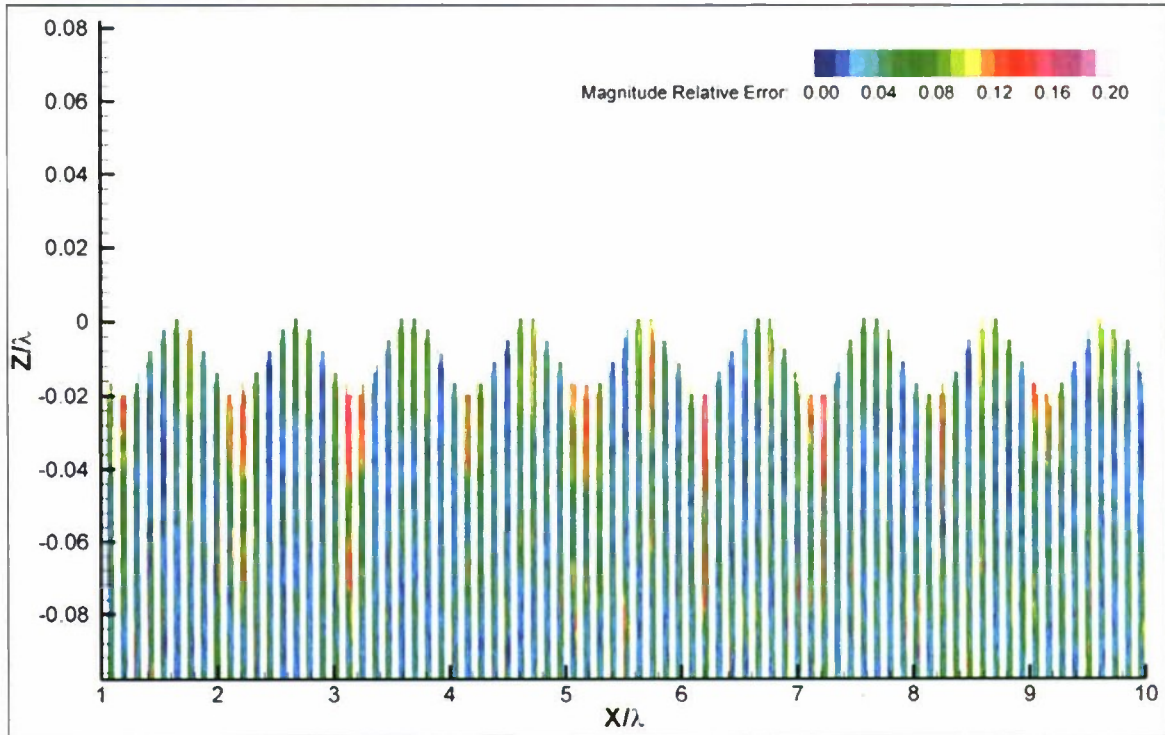
Figure 7. Plot of the relative error in velocity magnitude for regular waves with 1/50 wave steepness.
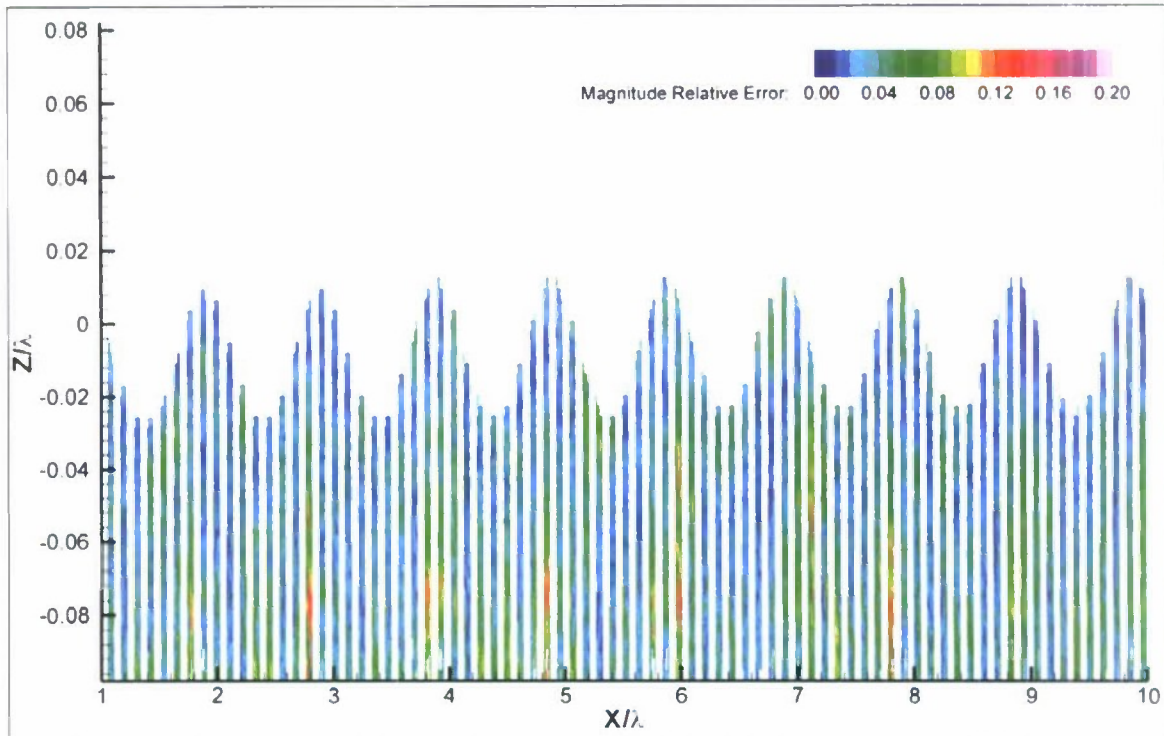
Figure 8. Plot of the relative error in veloeity magnitude for regular waves with 1/30 wave steepness.
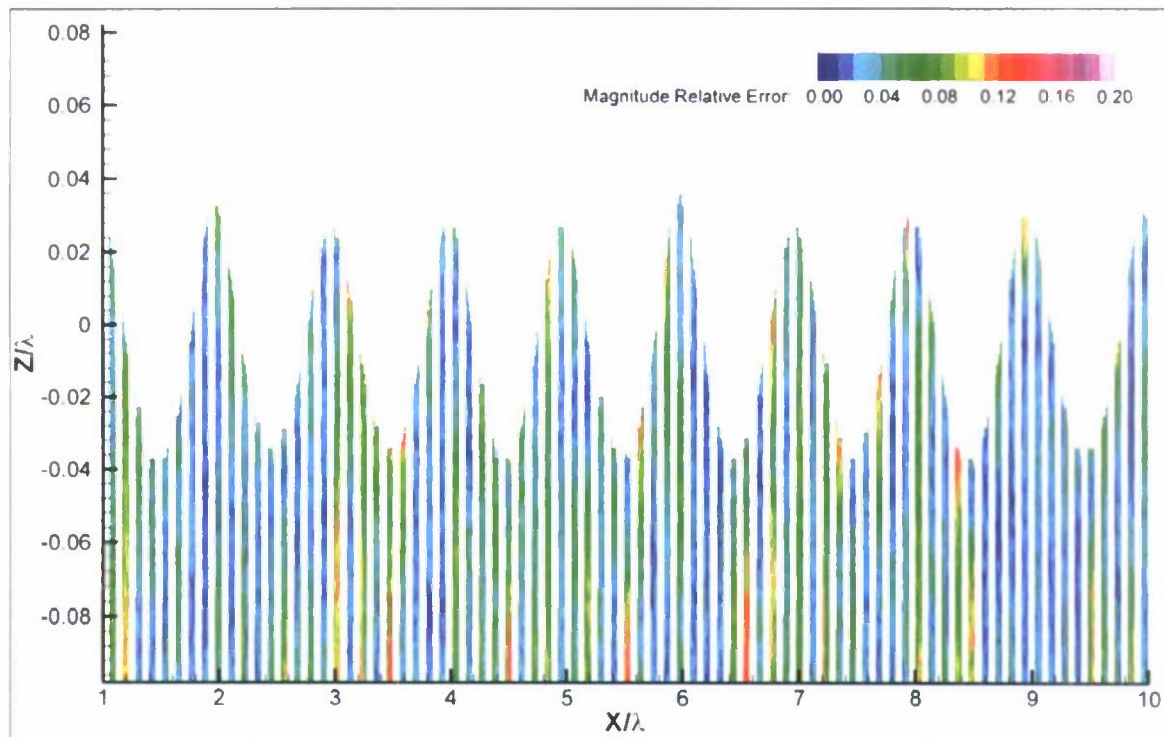

Figure 9. Plot of the relative error in veloeity magnitude for regular waves with 1/15 wave steepness.

23
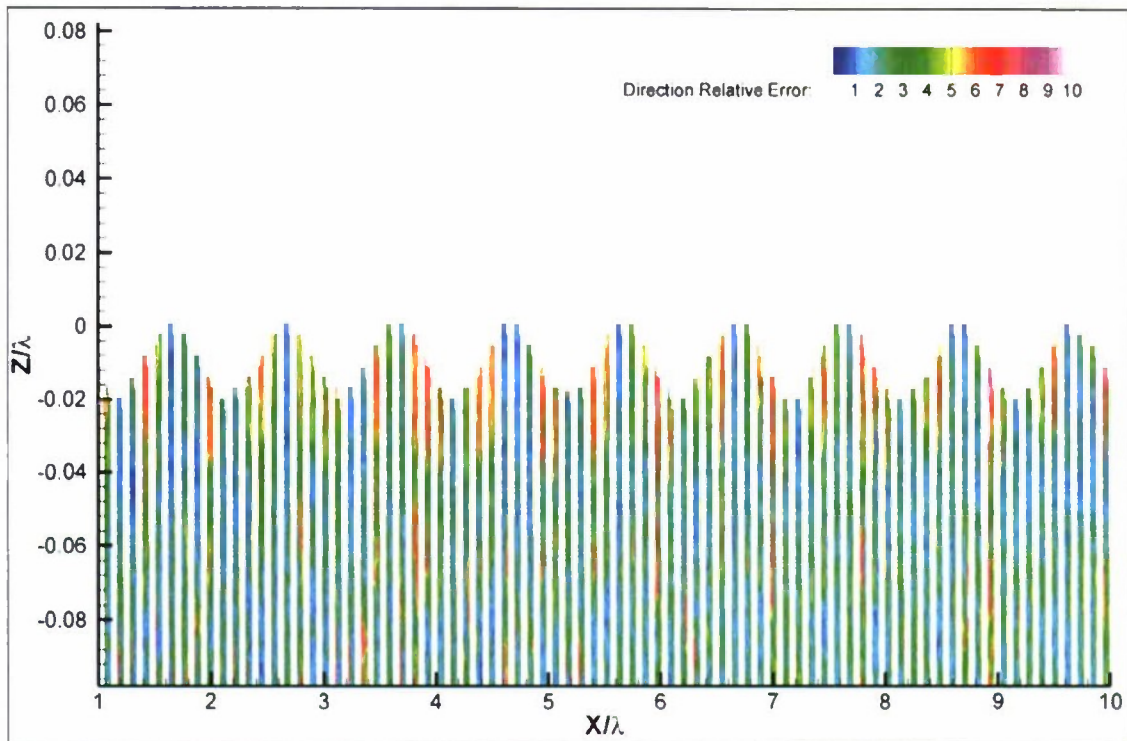
Figure 10. Plot of the relative error in velocity vector angle for regular waves with 1/50 wave steepness.
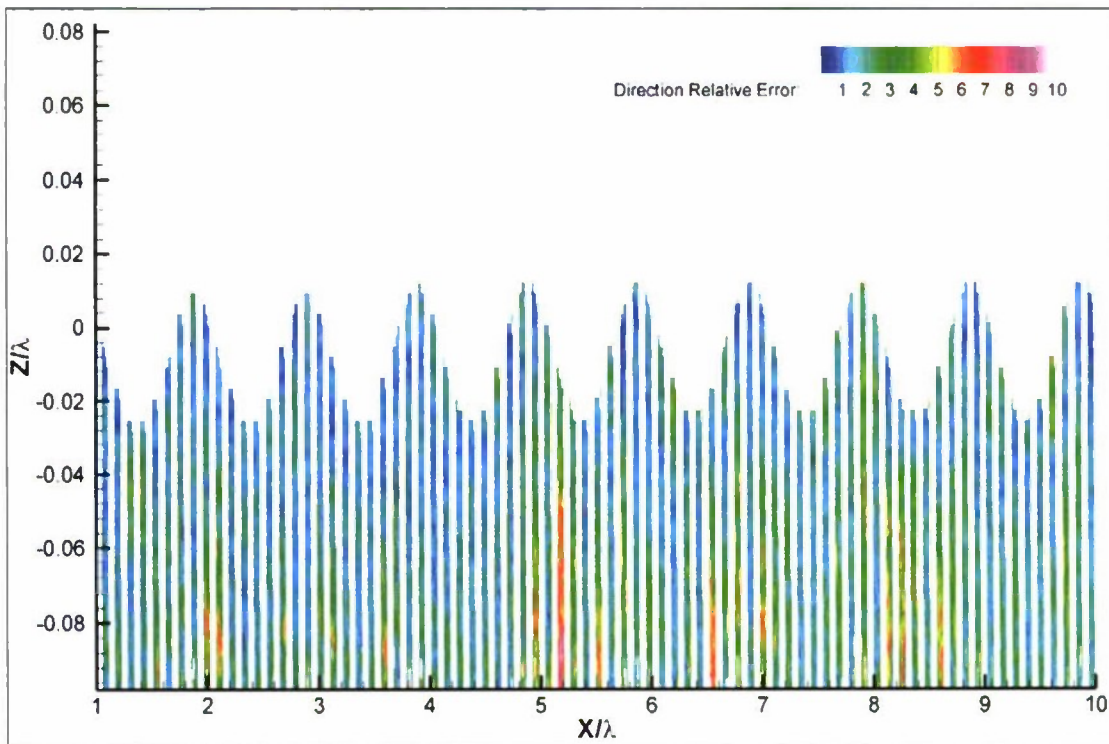
Figure 11. Plot of the relative error in velocity vector angle for regular waves with 1/30 wave steepness.

24
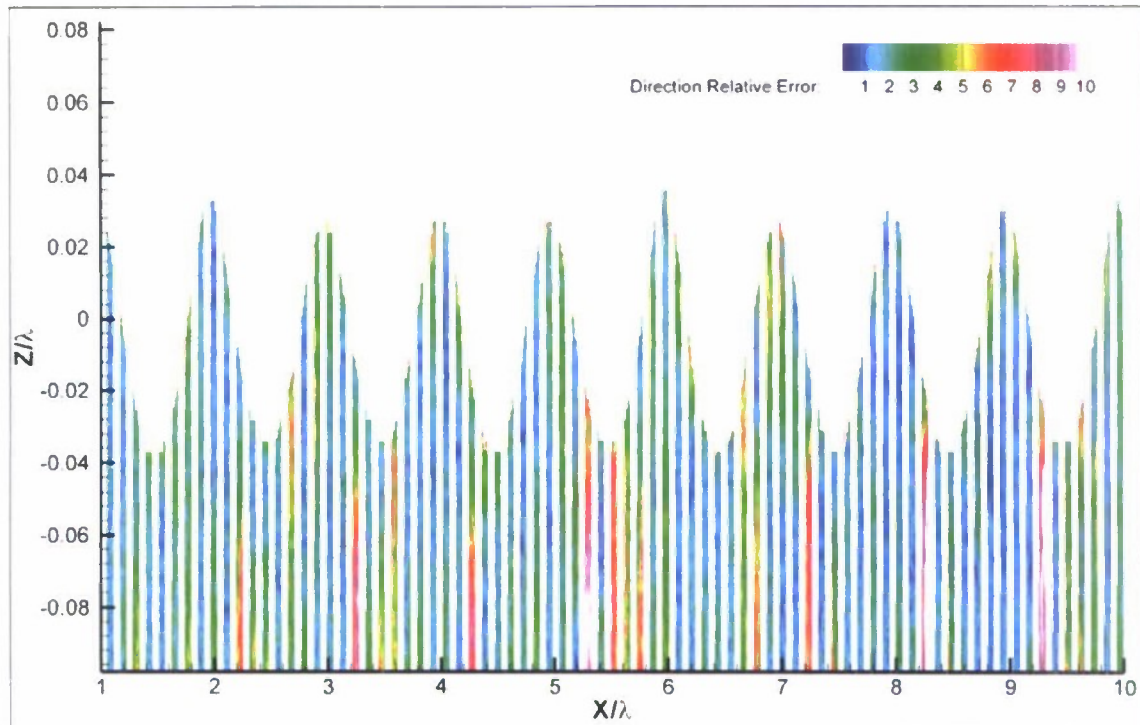
Figure 12. Plot of the relative error in velocity vector angle for regular waves with 1/15 wave steepness.

VELOCITY FIELD MEASUREMENTS AND DATA PROCESSING

Figure 13 shows an example of a raw PIV image (A) and a masked image (B). The bright white line spanning the image from left to right is the free surface. Above this line in the image, is a reflection of the particles, which are illuminated beneath the free surface of the wave. Raw images were processed in MATLAB to create masked images that were imported and processed using *La Vision* DaVis software v7.2. A multi-pass processing technique was used and the vectors were median filtered, zeroing vectors whose magnitudes were greater than 2.5 times the rms value of neighboring vectors. Interpolation or filling of blank spaces in each processed image was not performed.

Figure 14 shows the resulting velocity field calculated by DaVis for a given image pair. The origin is defined at the center of the PIV measurement plane (x=0, z=0). Each image is 2048 x 2048 pixels in size and the images are processed in pairs. In the first processing pass the image is divided into interrogation windows 64 x 64 pixels in size. A cross-correlation scheme is then applied resulting in a velocity vector for each interrogation window. Two additional passes, each using 32 x 32 pixel interrogation windows, are then completed building on the information gained from the previous pass. Each velocity vector represents the solution for a given interrogation window and shows the magnitude of the velocity and direction at a given point in the flow field resulting in a velocity vector field of 64 x 64 vectors.

25
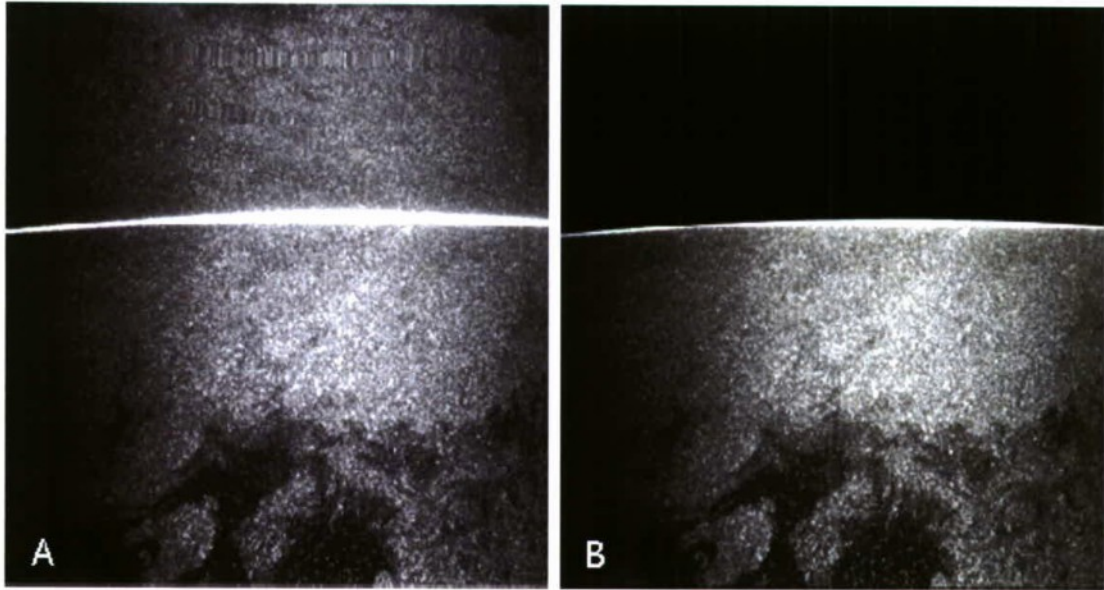
Figure 13. Raw (A) and masked (B) PIV images with particle seeding in the wave-field below the free surface.
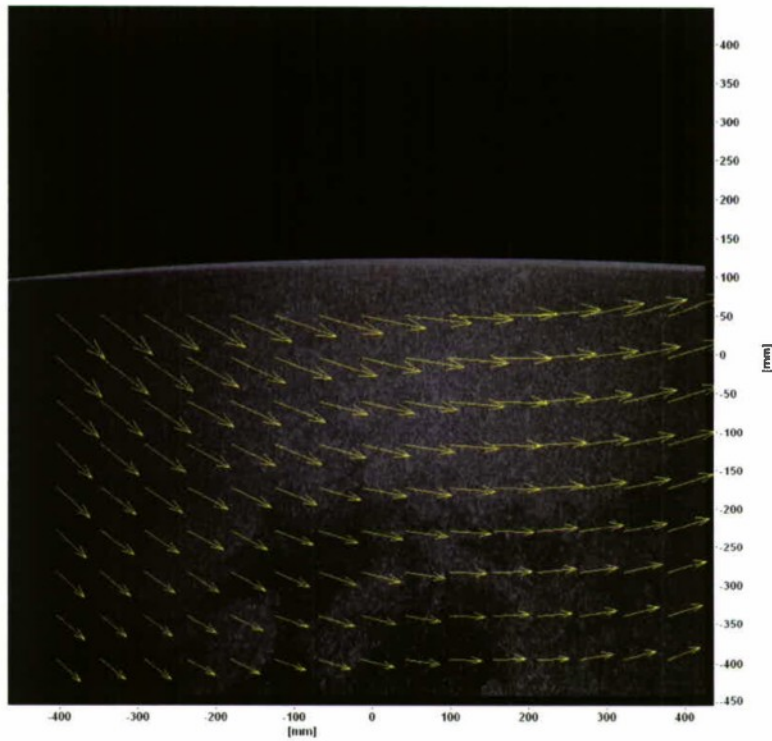

Figure 14. Example of a processed PIV image showing calculated velocity vectors (in yellow) for regular waves, H/λ=1/30; for clarity, only every 4th vector is shown.

26

RESULTS

A comparison of wave height data from the ultrasonic wave probes and PIV images as well as wave field kinematics results for regular and irregular wave measurements is presented. For comparison, the data is normalized by the reference velocity, V_{REF}, and wavelength, λ. The deep-water wave celerity, for the reference wavelength of 4.81m, was used as the reference velocity, V_{REF}=2.74 m/s, for all cases.

Regular wave analysis includes a comparison of experimental velocity profiles to theory (for one wave period), and velocity contour plots for each wave steepness over three wave periods. For the irregular wave conditions, an analysis of the embedded groups is presented with a focus on the effect of group location, group composition, and scaling on the kinematics of the group. PIV images pairs were taken every 200ms. For the regular waves conditions one wave period traveled through the PIV measurement plane in approximately 1.76 sec and each processed image pair captured approximately 18.6% of the wavelength, with approximately 39% overlap between successive images. A preliminary assessment of the results from the experiment was reported in Minnick, et al. (2010).

Wave Surface Elevation Measurements

As seen in Figure 13 information about the free surface can be gained from the PIV images. A comparison between the ultrasonic wave probe data and the free surface elevations determined from the PIV images is shown for regular waves with a steepness of 1/15 (Figure 15) and irregular waves (Figure 16). For each PIV image, the free surface was defined using a 2nd-order polynomial interpolation scheme. The ultrasonic wave probes provide a point measurement, while the PIV images provide free surface information for a 0.895m (2.9 ft) segment of the wave, at a given moment in time

Figure 15 provides a comparison of the two measurements of the free surface for the H/λ=1/15 regular waves condition. The "steps" in the ultrasonic wave probe data observed at x/λ=4, 4.5, and 4.9 show a limitation of the ultrasonic wave probes for the measurement of steep waves. If a wave becomes too steep, the signal return angle becomes too large for the ultrasonic wave probe to receive and record a measurement. When this occurs, the ultrasonic wave probe continues to output data from the last received return signal until receiving a new measurement (for additional discussion, see Smith, et al., 2007). The free surface information gained from the PIV images is a useful supplement for these measurement dropouts.

Figure 16 shows an embedded wave group in a BS-SS8 seaway. The steps seen in the ultrasonic wave probe data around x/λ=24.5 (t=83) and x/λ=25 (t=84 sec) again show the limitation of the ultrasonic wave probes for measurement of steep waves. The free surface information from the PIV images does not form a continuous line because, for each 0.895m (2.9 ft) segment, the free surface is continually changing. For a strict comparison, only the point in the segment that corresponds to the location of the ultrasonic probe would be plotted. The effect is usually small, however, and the overlapping segments are useful for visualization.

Overall, the free surface data from the PIV images agree well with the ultrasonic wave probe data. It is shown that combining the two measurements can provide a more

27

complete picture than either measurement alone. The free surface data collected by the PIV images is helpful in providing free surface measurements in the data gaps experienced by the ultrasonic wave probes during steep waves.
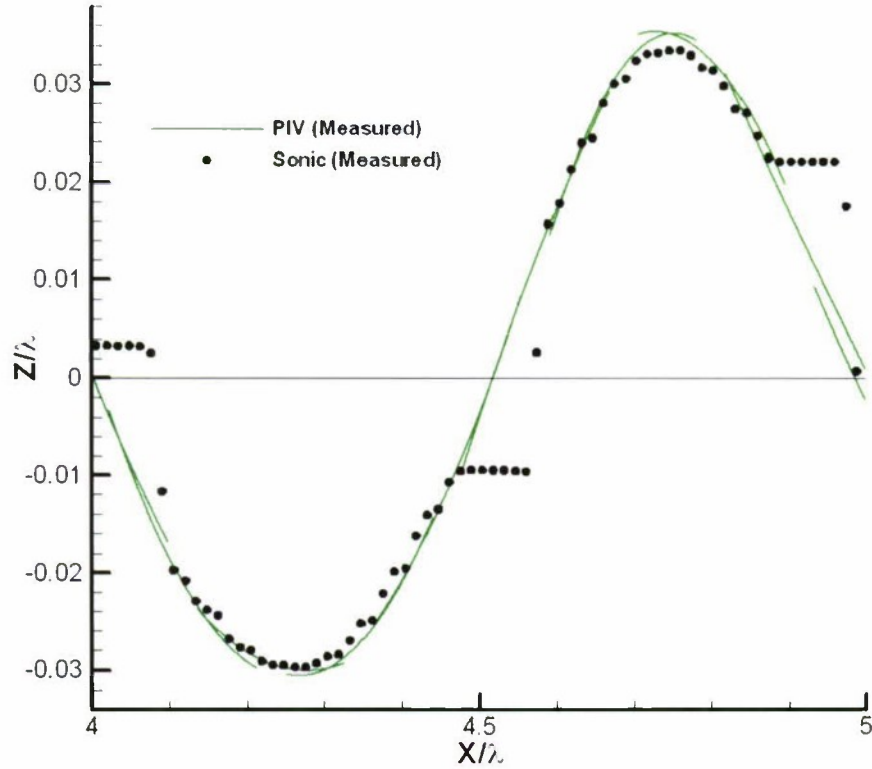
Figure 15. Regular wave, 1/15 steepness, free surface elevation time-history from MASK basin wave probe 3 (black dots), PIV free surface interpolation (green line).
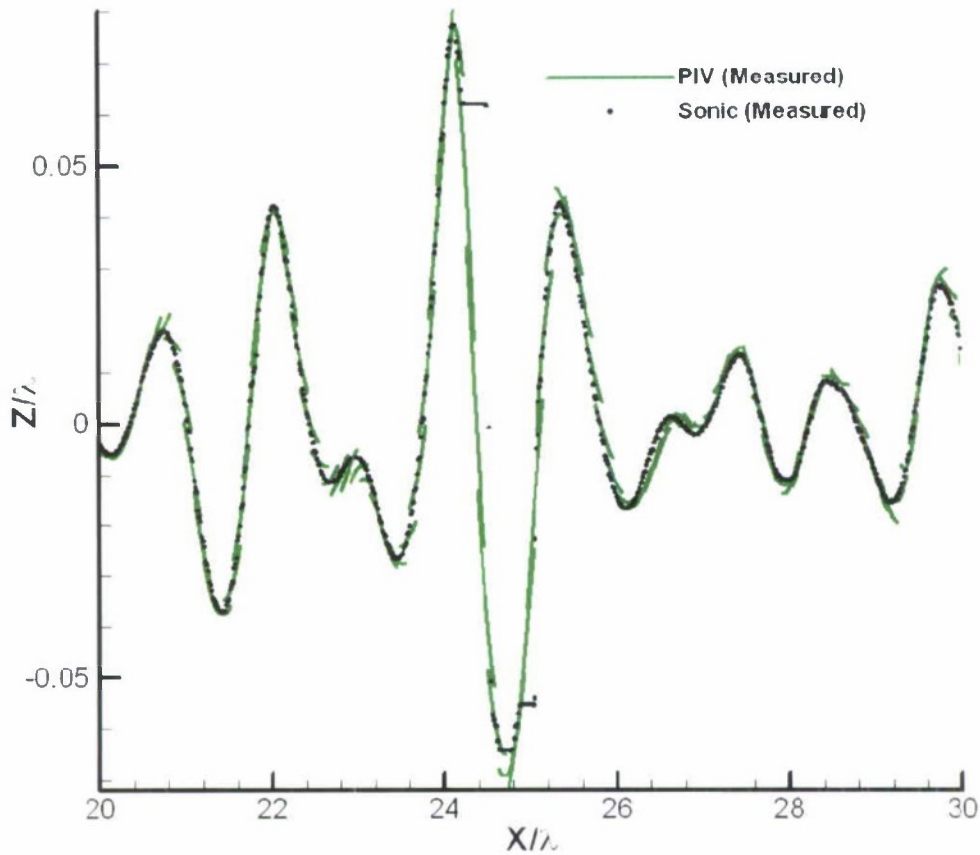
Figure 16. Irregular wave with embedded wave group, BS-SS8, free surface elevation time-history from MASK basin wave probe 3 (black dots) and free surface data from PIV images (green line).

Regular Waves

Table 6 summarizes the runs collected in regular waves. Each spot captured 28 wave cycles. The time histories for wave probe 3 for the spots listed in Table 6 are shown in Appendix A. The time histories show the repeatability between spots as well as the repeatability of the sine wave within a spot. It is important to note the quality of the 1/15 waves. For the specified wavelength of 4.81 m, these waves are near the limits of the wave-maker and the limits of the wave probes used to measure the free surface. Therefore, the repeatability from 1 cycle to the next is not as good as for waves of smaller steepness.

Table 6. Regular wave runs.

Spot #	H/λ	Height, inches	Height, mm
10	1/50	3.79	96.2
11	1/50	3.79	96.2
4	1/30	6.31	160.3
5	1/30	6.31	160.3
54	1/15	12.62	320.7
55	1/15	12.62	320.7

*λ=4.81 meters

Figure 17 - Figure 19 show a comparison of the measured free surface profile modeled with linear theory and 2nd-order Stokes wave predictions. Details of linear theory and 2nd-order Stokes can be found in Appendix B. While the generation of regular waves in an experimental basin is based on the input of sine functions to a wave-maker, as the generated waves progress, non-linear effects are introduced and the shape deviates from a perfect sine wave. Specifically, the waves develop sharper crests and flatter troughs. This deviation from a sine wave becomes more significant as a wave approaches breaking, which occurs at approximately 1/7 steepness.

The onset of this effect may be observed in the 1/15 steepness waves (Figure 19), the amplitude of the wave crest and trough are different; the trough is shallower than the wave crest. Linear theory over-predicts the trough, but corresponds well with the ultrasonic data at the crest while 2nd-order theory agrees with both PIV free surface and ultrasonic data at the trough and corresponds more with the PIV free surface data at the crest. The best correlation with linear theory is seen in the 1/30 steepness waves (Figure 18). The trough of the 1/50 waves corresponds with theory but the actual wave crest is higher than both linear and 2nd-order theory. This may be due to the limitations of the pneumatic wave-maker. Waves of 1/50 steepness, at the given wavelength, approach the smallest waves that can be consistently produced in the MASK facility. It is possible the waves are so small that any non-linear effects are more prevalent, causing a sharper peak than predicted. However, more investigation must be done to fully understand the issue.
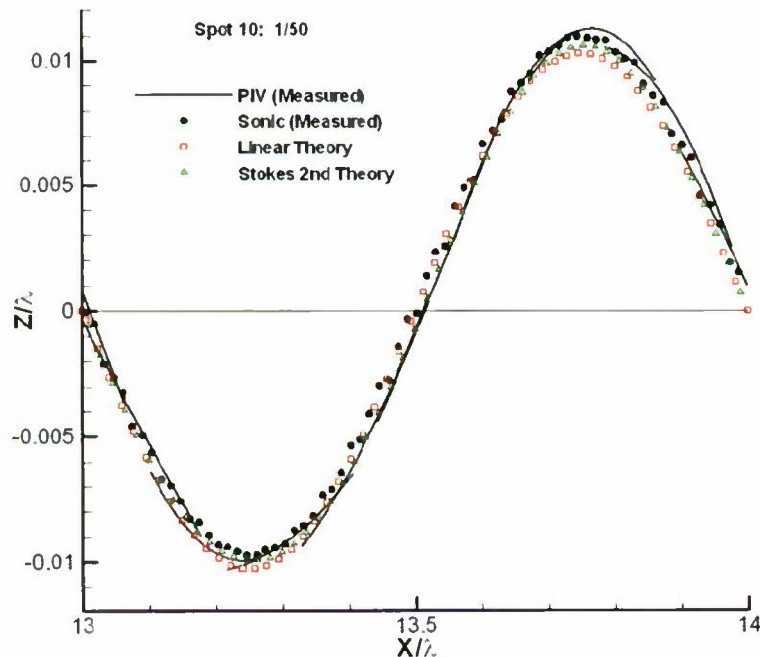

Figure 17. Regular wave, 1/50 steepness, free surface elevation time-history from MASK basin wave probe 3 (black dots), PIV free surface interpolation (black lines), with comparisons to linear (red squares) and 2nd-order Stokes (green triangles) wave theory predictions.
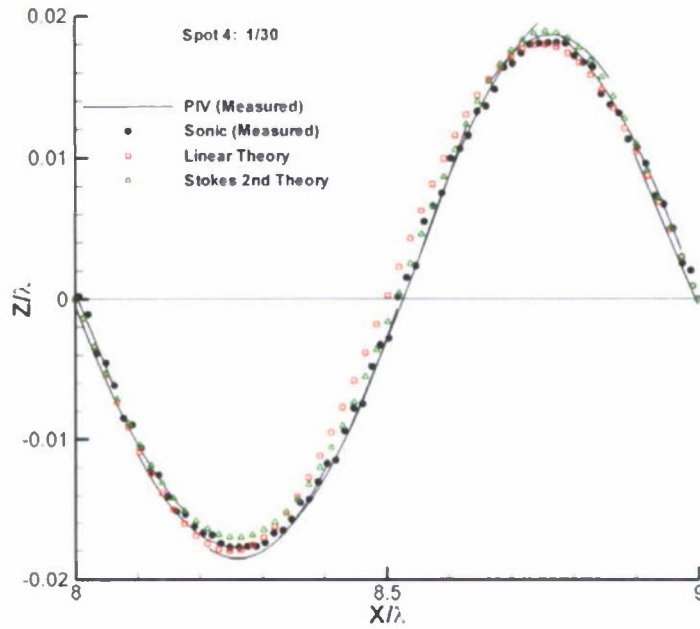
Figure 18. Regular wave, 1/30 steepness, free surface elevation time-history from MASK basin wave probe 3 (black dots), PIV free surface interpolation (black lines), with comparisons to linear (red squares) and 2nd-order Stokes (green triangles) wave theory predictions.
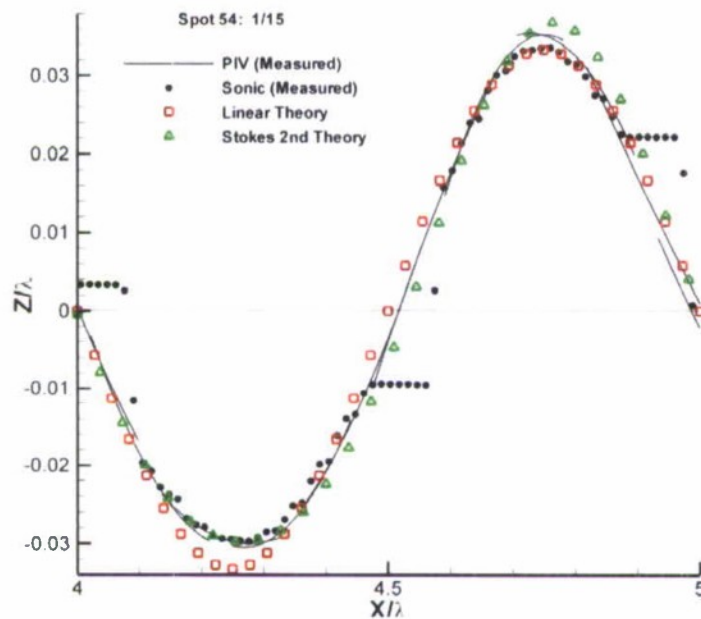

Figure 19. Regular wave, 1/15 steepness, free surface elevation time-history from MASK basin wave probe 3 (black dots), PIV free surface interpolation (black lines), with comparisons to linear (red squares) and 2nd-order Stokes (green triangles) wave theory predictions.

Figure 21-Figure 23 show the theoretical and experimental velocity profiles for each regular wave case. The lettering corresponds to successive PIV image pairs spanning one wave period, from crest to crest, as shown in Figure 20. Profiles A and I represent velocity profiles taken at the successive wave crests and profile F, the wave trough. The theoretical velocity profile is calculated using equation B-5 (Appendix B) using the average wave amplitude for a given time history. Each lettered velocity profile in the figure represents the experimental velocity profile at x=0 in the PIV measurement plane for a given PIV image pair.

Overall, as predicted by theory, the velocity is highest just below the free surface and decreases with increasing depth. In addition, the velocity magnitudes and velocity gradients in the wave-field increase with increasing wave steepness. The velocity profiles across the wave-field measurement plane, for a given time, also show greater variation with increased steepness and all exhibit an exponential trend. This exponential trend becomes more prominent as wave steepness increases.

Small amplitude wave theory (Appendix B) predicts a constant velocity magnitude for a given depth below the calm water free surface across all phases of the wave. Because the experimental waves are not an idealized periodic sine function, the experimental velocity profiles exhibit some variation. The greatest variation can be seen in the 1/15 wave steepness case. Figure 23 shows two distinct clusters among the velocity profiles: profiles A, B, H, and I, or those near the wave crest, and profiles C, D, E, F, and G, those near the wave trough. As wave steepness increases, the innate characteristics of experimentally generated waves (sharper peaks and flatter troughs) become more evident. The variation in amplitude between the wave crests and troughs increases resulting in two distinct trends as shown.

This can also be seen in Figure 24 - Figure 26, which show the velocity contours for 1/50, 1/30, and 1/15 wave steepness conditions, respectively. These plots were generated by taking a slice at x=0 of each successive PIV image. The total velocity vectors for each image at the x=0 slice are superimposed onto the contour plot. To enable better visualization, the presented contour plots have been distorted. Specifically, the x-axis has been compressed relative to the y-axis. Due to this compression, the steepness shown in the plots does not correspond to the actual steepness of the generated waves. Figure 27 and Figure 28 are presented to provide an example of an undistorted plot. In these figures the wave height is not non-dimensionalized and the x-axis represents the distance (in meters) the wave travelled since the beginning of the data collection.

Within a given figure, a longer velocity vector indicates a larger velocity magnitude. The scaling of vectors varies among Figure 24 - Figure 26 (for visualization purposes), but the color contours are consistent and can be used to make comparisons. While the velocity profiles presented show some variation in velocity for a given depth, the relatively horizontal contours for 1/30 and 1/50 wave steepness show the variation is small. However, the steepest regular wave condition, 1/15, shows a greater range of velocities throughout the same measurement plane and the contours begin to show more variation across the wavelength, specifically the contours begin to deviate from the relatively horizontal contours of the 1/50 and 1/30 wave steepness conditions.
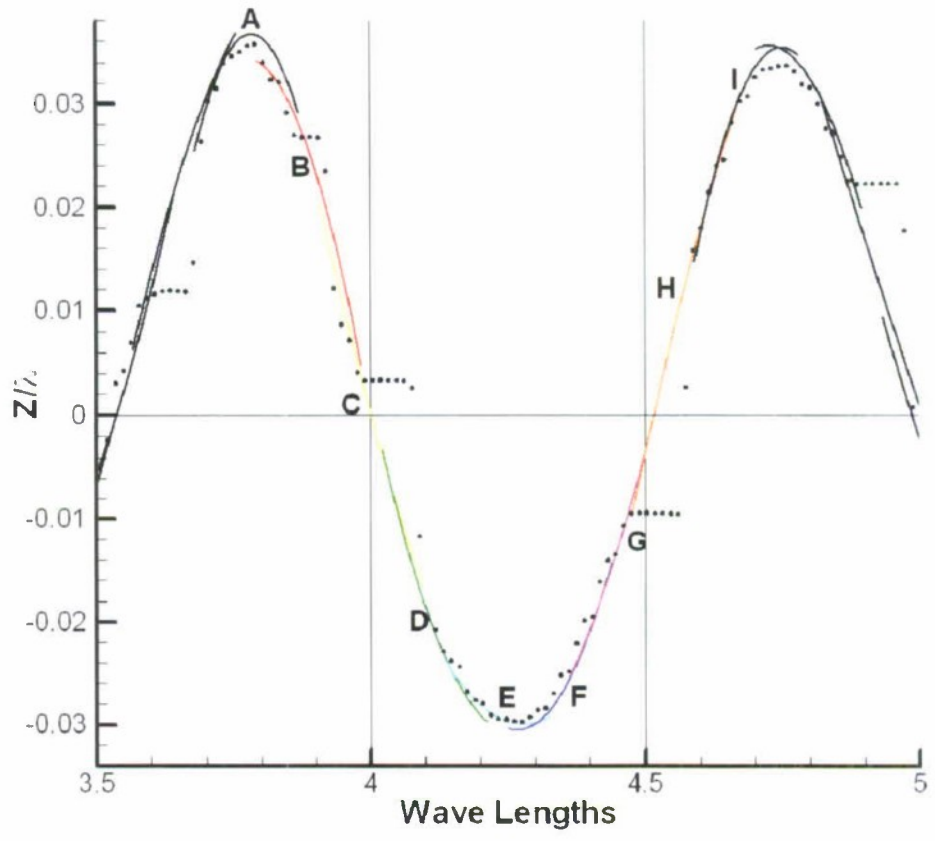
Figure 20. Free surface data of the regular waves, 1/15. MASK basin wave probe 3 (black dots) and free surface data from PIV images (black and colored lines).
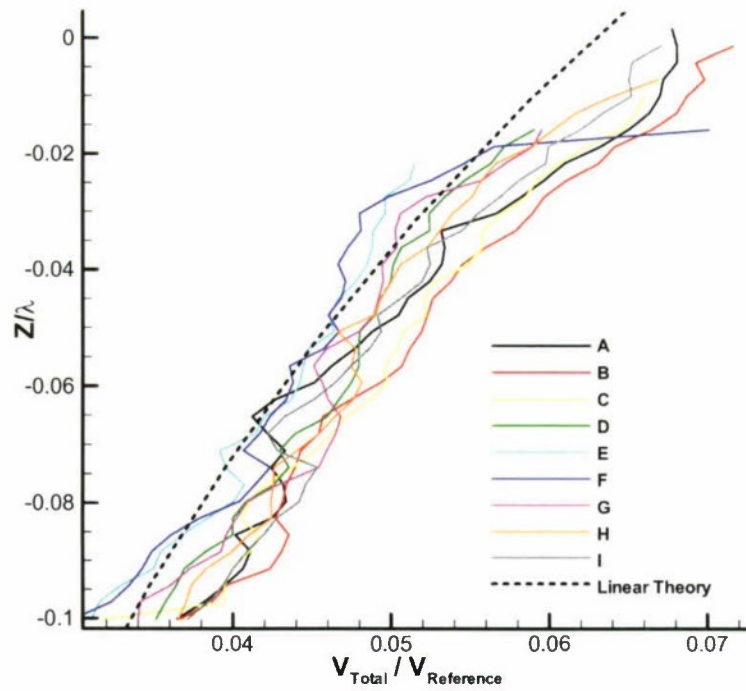
Figure 21. Theoretical and measured (for wave locations A-I) velocity profiles for regular waves, 1/50.
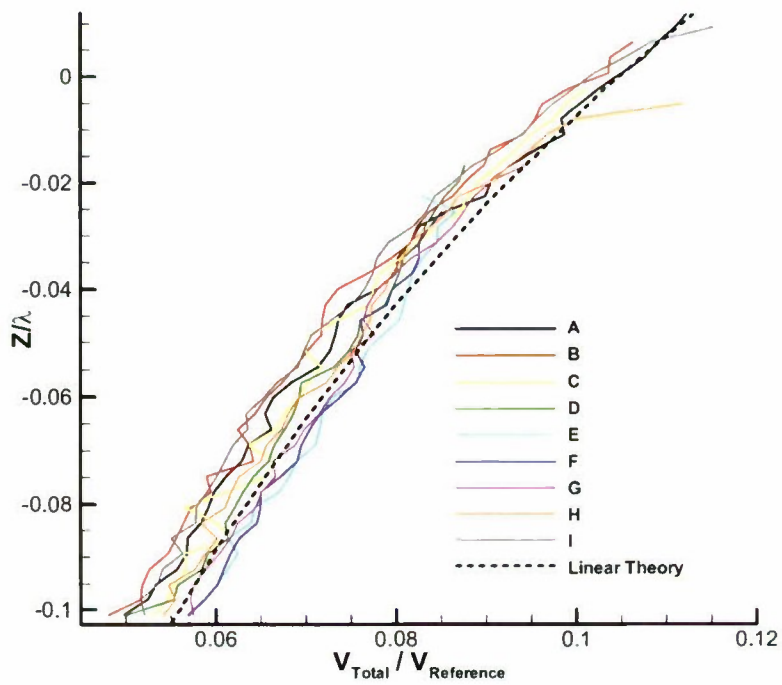
Figure 22. Theoretical and measured (for wave locations A-I) velocity profiles for regular waves, 1/30.
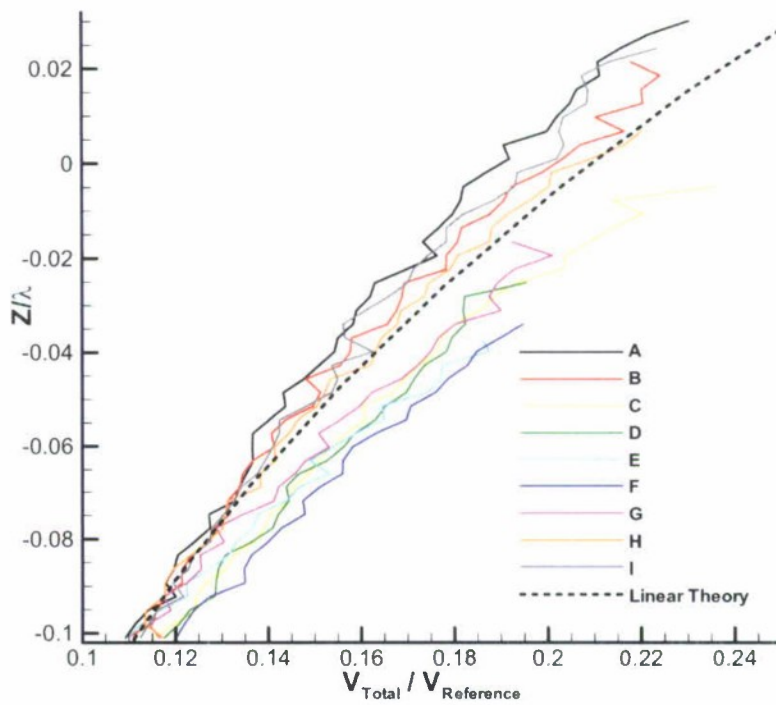
Figure 23. Theoretical and measured (for wave locations A-I) velocity profiles for regular waves, 1/15.
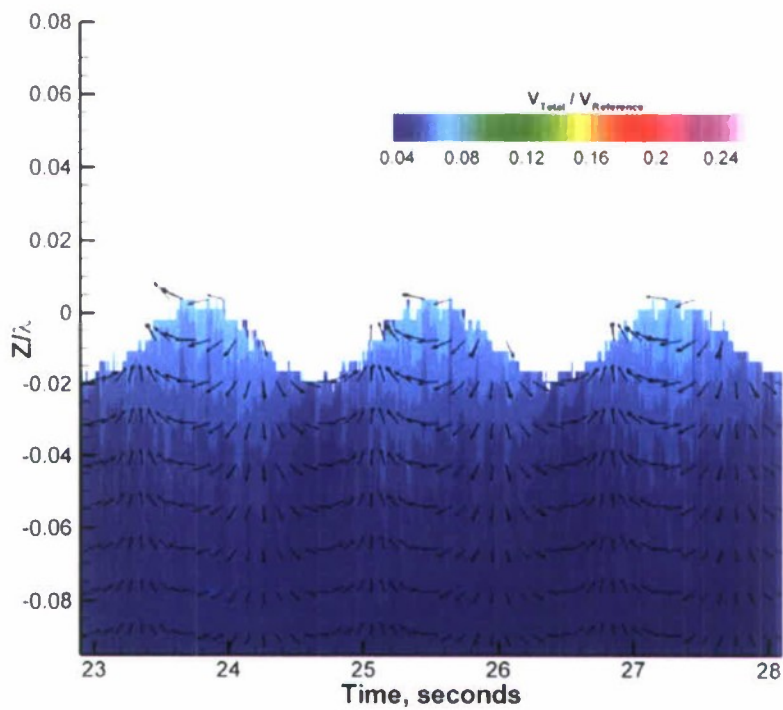
Figure 24. Total velocity contours for regular waves, 1/50 wave steepness.
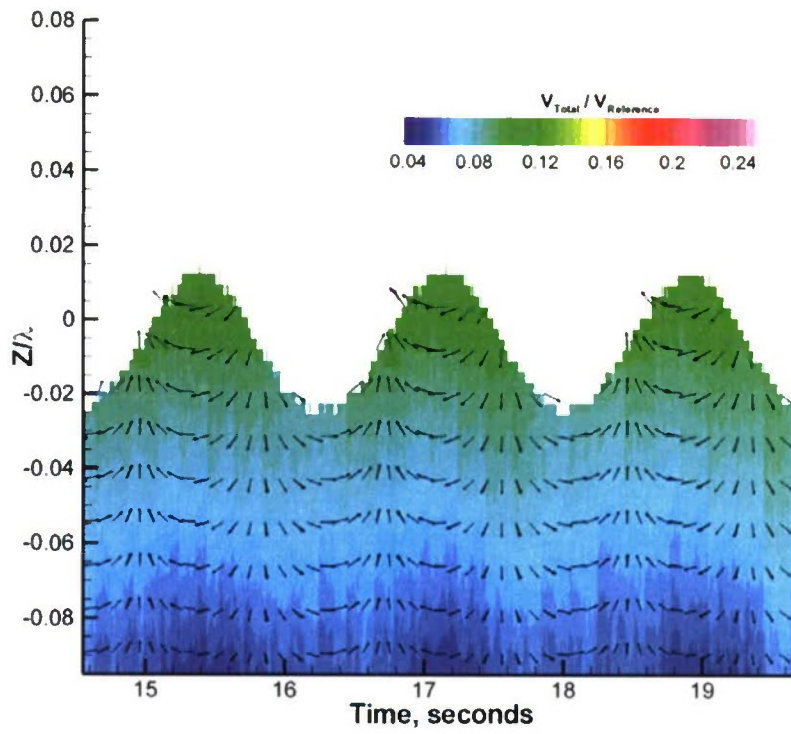
Figure 25. Total velocity contours for regular waves, 1/30 wave steepness.
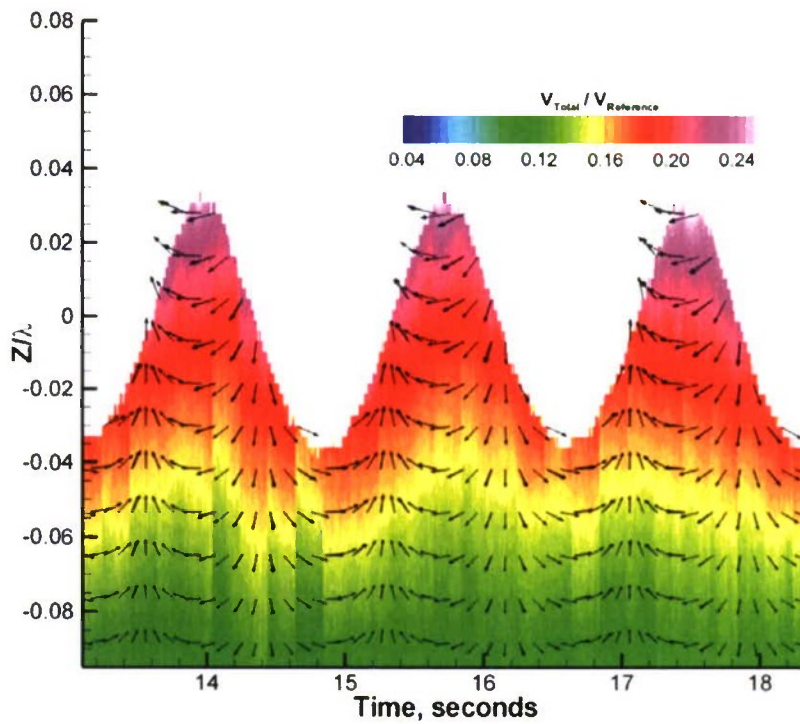
Figure 26. Total velocity contours for regular waves, 1/15 wave steepness.

36
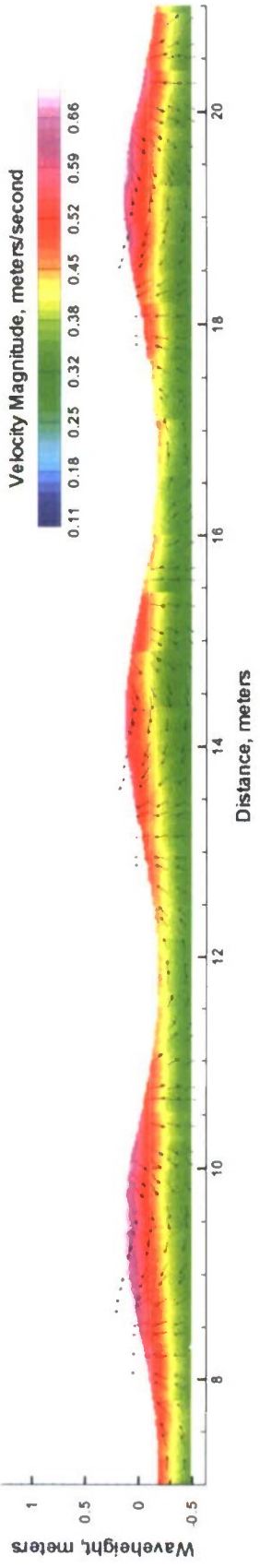
Figure 27. Undistorted plot of three wave crests of regular wave condition, 1/15 wave steepness.
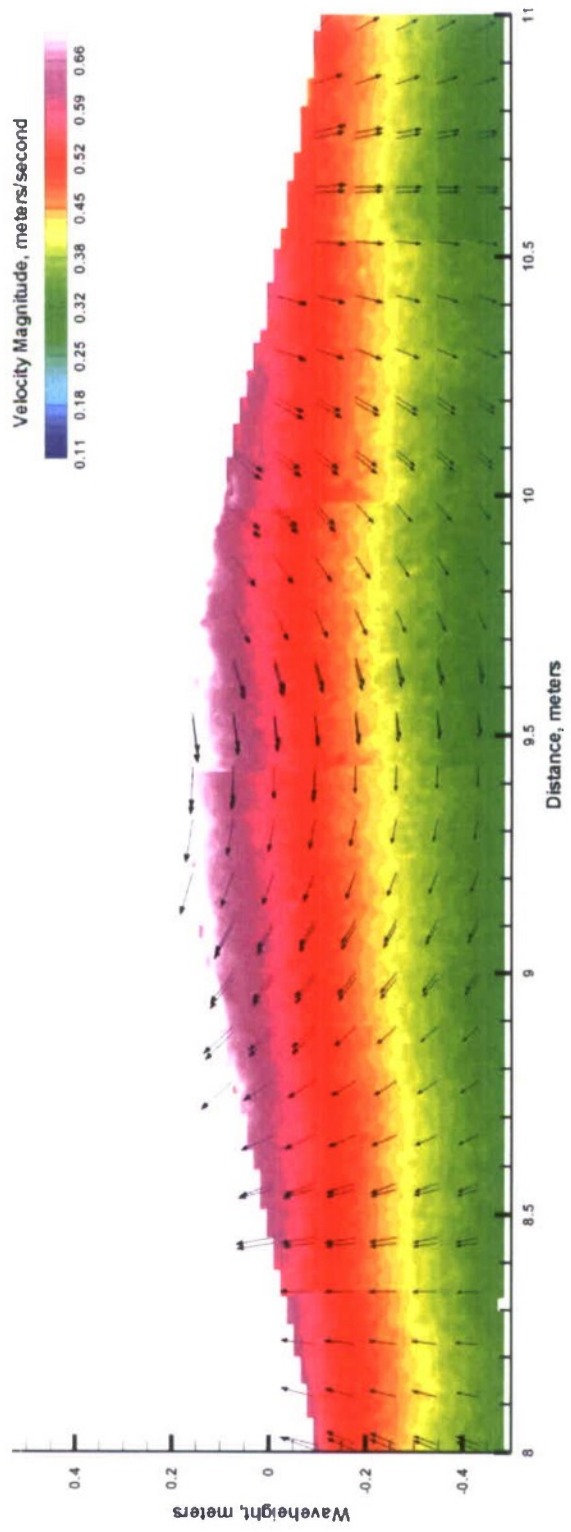
Figure 28. Undistorted plot of close-up of one wave crest for regular wave condition, 1/15 wave steepness.

37

This page intentionally left blank.

Irregular Waves with Embedded Wave Groups

Irregular wave conditions for the experiment included 30th and 46th scale realizations of Hurricane Camille and 30th scale Bretschneider Sea State 8 (BS-SS8) spectra, all with and without embedded wave groups. These conditions were first generated and examined in Bassler, et al (2008) as part of a feasibility study for examining the generation of deterministic wave groups in the MASK basin. This study continues that examination to also include wave kinematics measurements.

Two 30th scale Hurricane Camille realizations with an embedded group were examined; wave group 42 and wave group 43 (see Bassler, et al., 2008 for specifics on the generated wave groups). The location of the group within each realization is the same; however the composition of the group varies slightly. Wave group 44 was embedded in a 46th scale Hurricane Camille realization. Wave group 44 is similar in composition and location to wave group 42. In addition, two BS-SS8 realizations with an embedded wave group were examined; wave group 37 and wave group 38. Each realization is identical except the location of the wave group varies. Each run was repeated once. Table 7 summarizes the irregular wave test conditions. Time histories for wave probe 3 for each run are shown in Appendix C.

The time histories exhibit the repeatability of the runs and of the method to embed a distinct deterministic group within an irregular seaway. It was assumed the addition of the deterministic wave group would not affect, in a measurable way, the spectrum in which it was embedded. The spectral shape of each realization was monitored to confirm this assumption and no significant changes to the spectrum were observed.

Table 7. Summary of irregular wave conditions.

Condition	Hs inches	Hs mm	Tm sec	Total Time sec	Wave Group Start, sec
Camille 30th Scale					
Camille 30th-42	16	406.4	2.45	120	54
Camille 30th-43	16	406.4	2.45	120	54
Camille 46th Scale					
Camille 46th-44	10.3	261.6	1.96	120	60
BS-SS8					
BS-37	15	381	3	100	75
BS-38	15	381	3	100	42

Hurricane Camille

Figure 29 contains plots of the 46th and 30th scale Hurricane Camille realizations. The time histories are from wave probe 3. The wave groups are traced in red. The first plot in the figure is a realization with wave group 42, the second plot is a realization with wave group 43, and the third plot with wave group 44. All three wave groups occurred near the middle of the realization.
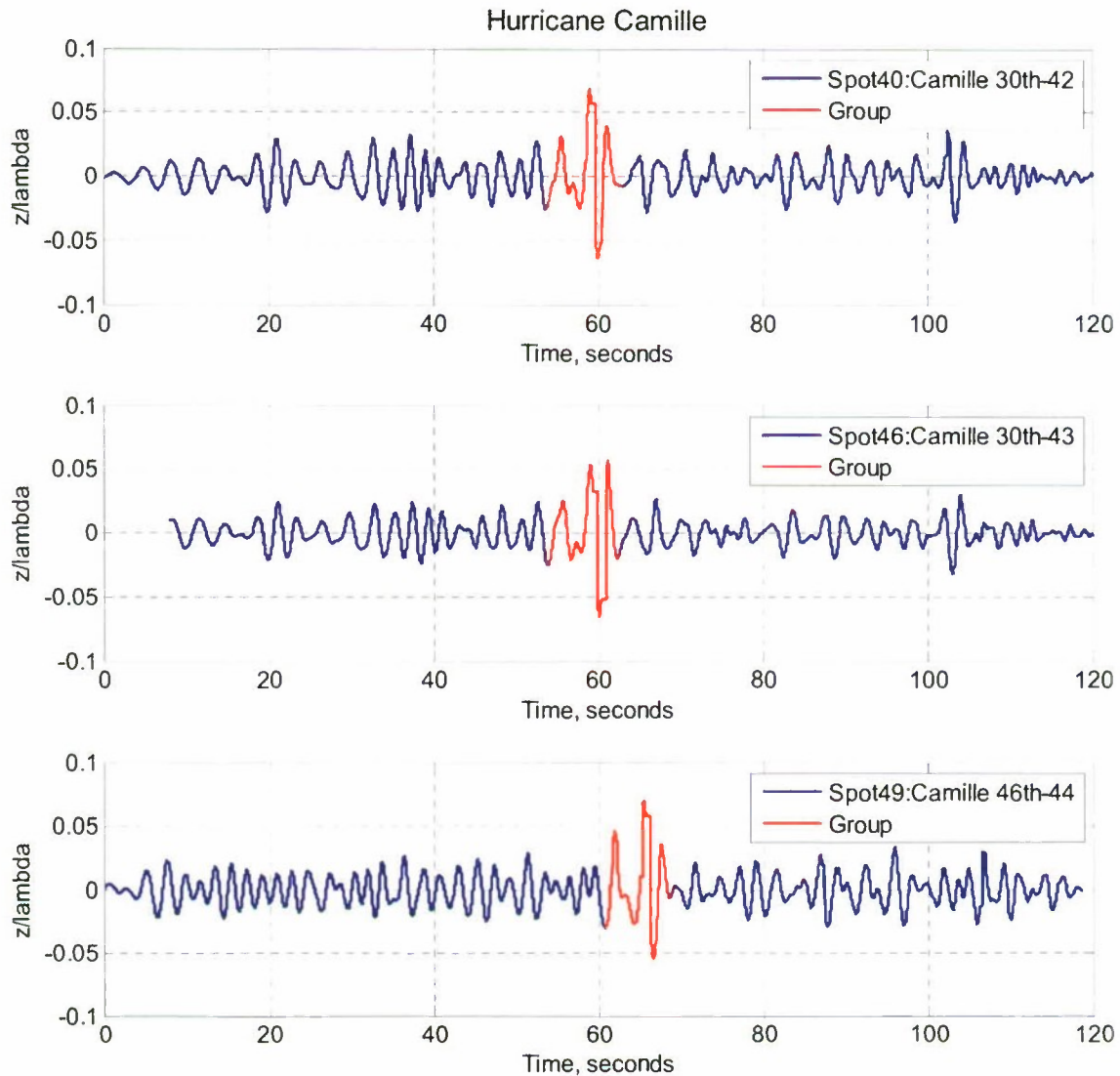
Figure 29. Hurricane Camille realizations with embedded wave groups. The red tracing indicates a wave group.

Wave group 42 and wave group 43 vary in wave group composition. Both wave groups consist of three waves. The first wave is the smallest, followed by two crests significantly larger in amplitude than the other waves in the time series. For wave group 42, the second wave is the largest and is followed by a third wave slightly larger than the first, but smaller than the second. This is in contrast to wave group 43 where both the second and third waves are of approximately equal amplitude

Figure 30 and Figure 31 show a long snapshot of wave groups 42 and 43, respectively, while Figure 32 shows a side by side comparison of the velocity contours of wave groups 42 and 43. These plots were generated by taking the x=0 slice of each successive PIV image. The total velocity vectors for each image at the x=0 slice are superimposed onto the contour plots. The wave height is not non-dimensionalized and the x-axis represents time, with zero seconds equal to the beginning of the data collection. The presented plots are in the reference frame of the PIV camera, where the waves are

moving right to left. The x-axis has been compressed for visualization purposes and therefore, the relative steepness among waves has been distorted. Figure 33 and Figure 34 show undistorted plots of the second and third crest of wave group 42 and 43 respectively. In these plots, the wave height is not normalized and the x-axis represents the distance (in meters) the wave has travelled since the beginning of the data collection.

Overall, instead of relatively even-layered and symmetric velocity contours, as observed in the regular wave measurements, the velocity contours for the group are more chaotic and asymmetric. The velocity contour plots also demonstrate that unlike the regular wave conditions, the velocity field for the wave group varies with phase. The regular wave conditions showed a strong dependence of the velocity on depth, but little dependence on position within a wave. Almost the opposite is seen for the irregular cases.

The velocity contours for the second and third waves have distinctly different characteristics than the regular waves, even the steepest case of 1/15. A "U-shaped" region of highest velocity is observed between the peaks of the second and third waves. The high velocity region on the backside of the second wave crest continues to the front of the third wave. This is an example of the deep water dispersion relation and the effect of the wave generation method used in this experiment. As a result of dispersion, lower frequency waves travel faster than higher frequency waves. The "U-shaped" region illustrates the "over-taking" of a slower wave by a faster one, as the group is temporarily formed and then dispersed. If this velocity field is similar in structure to full-scale ocean wave groups then this, along with the initial conditions at the time the ship encounters the wave group, may significantly contribute to the severity of the response for a ship encountering the wave-field. Figure 35 shows the time history from wave probe 3 of a 30th scale Hurricane Camille realization without an embedded group. At approximately 30 seconds, successive waves in the time history resemble a group structure similar to the generated wave groups. Figure 36 shows the velocity contour plot of a portion of the time history presented in Figure 35. Overall, the kinematics of the indigenous group from the irregular seaway realization are similar to those of the generated group shown in previous figures. This provides some indication that the wave group generation method used does not significantly influence the measured kinematics.

The difference in group composition can be seen in Figure 32. The first wave in each group is similar; however the second wave is larger in group 42 than in group 43. The larger wave in group 42 leads to a smaller third wave and the highest velocities are concentrated in the face of the crest of the second wave. This is in contrast to wave group 43 where the second and third waves are similar in height and the highest velocities are seen both coming down the crest of the second wave, through the trough, and up into the crest of the third wave with a higher concentration of maximum velocities in the third wave rather than the second.

This page intentionally left blank
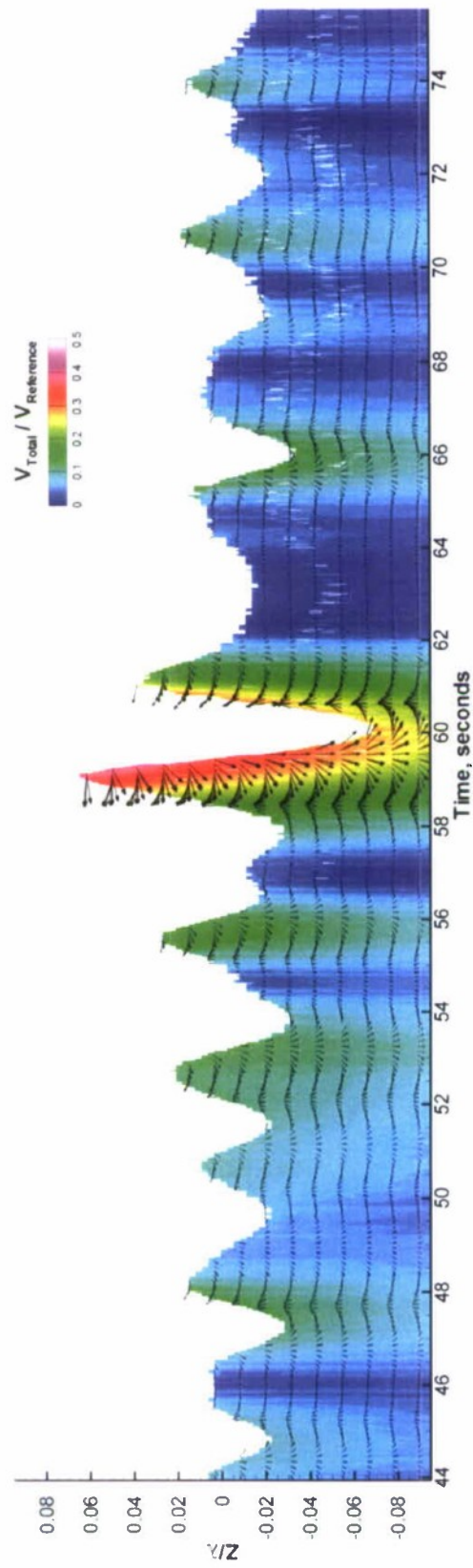
Figure 30. Velocity contour plot with total velocity vectors for wave group 42 embedded in a 30th scale Hurricane Camille spectrum, distorted.
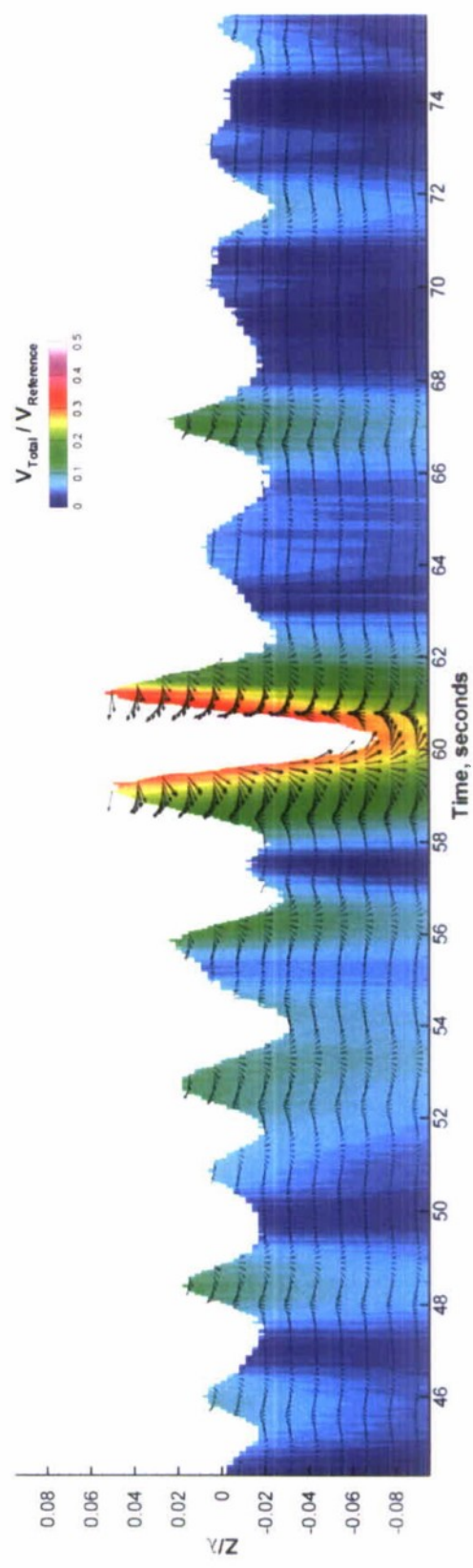
Figure 31. Velocity contour plot with total velocity vectors for wave group 43 embedded in a 30th scale Hurricane Camille spectrum, distorted.

43
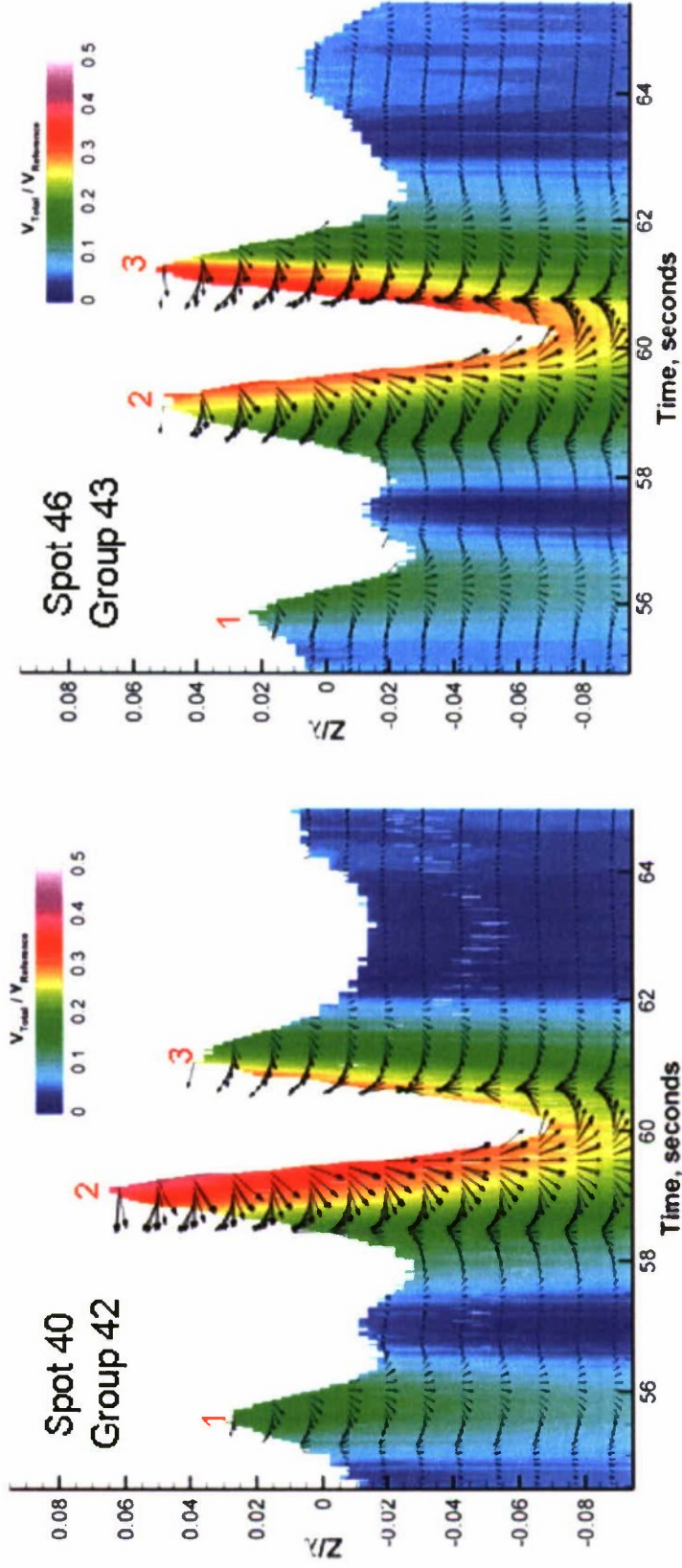
Figure 32. Velocity contour plots with total velocity vectors for wave group 42 and wave group 43.
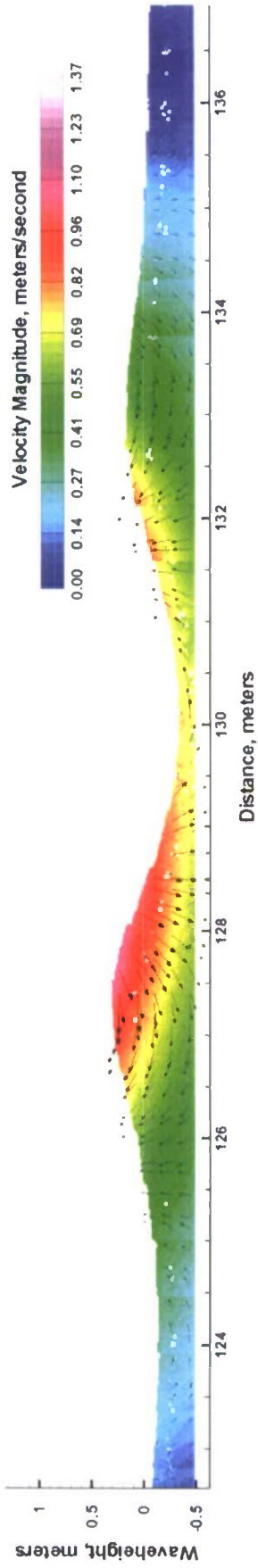
Figure 33. Velocity contour plot with total velocity vectors for wave group 42 embedded in a 30th scale Hurricane Camille spectrum, undistorted.
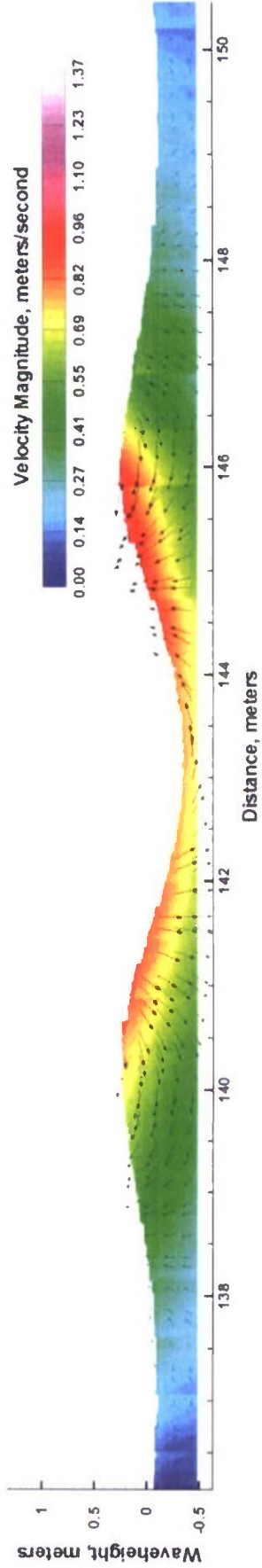
Figure 34. Velocity contour plot with total velocity vectors for wave group 43 embedded in a 30th scale Hurricane Camille spectrum undistorted.
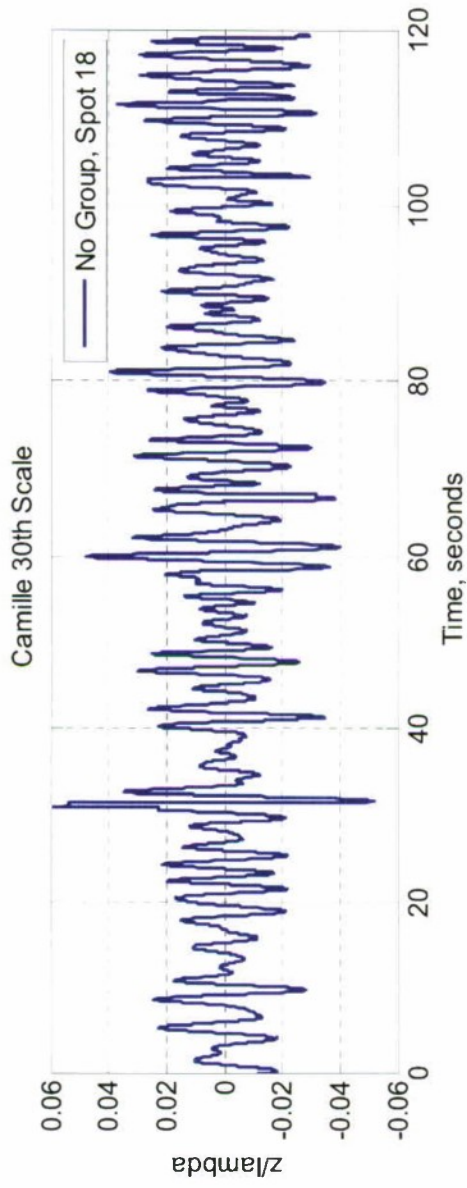
Figure 35. Time history from wave height probe 3 of 30th scale Hurricane Camille realization with no embedded groups.
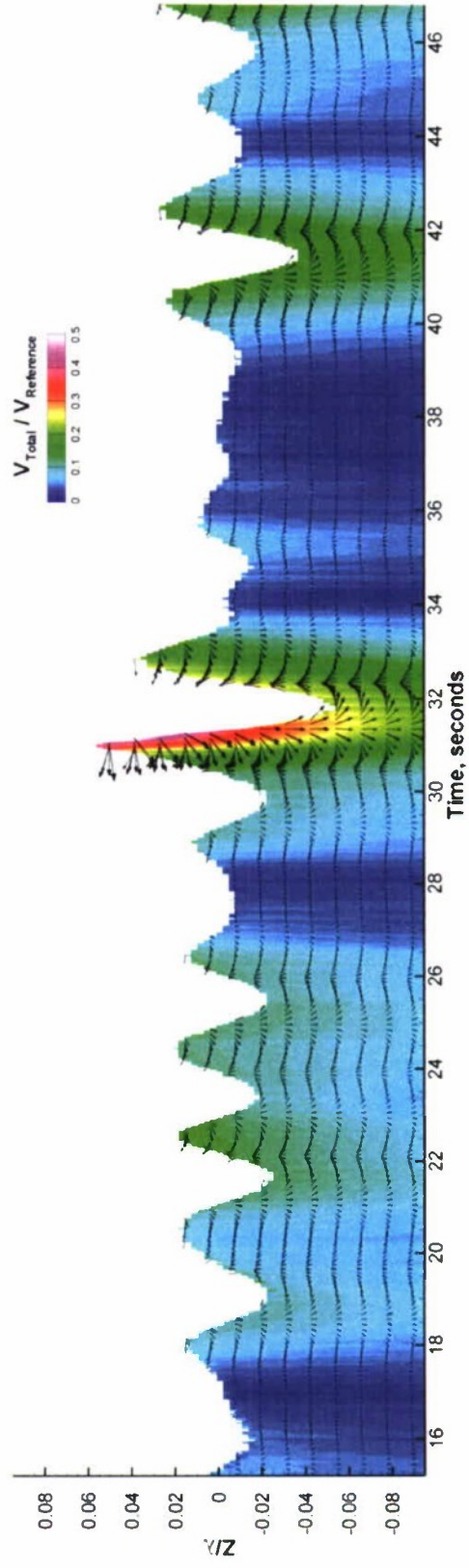
Figure 36. Velocity contour plot with total velocity vectors for a 30th scale Hurricane Camille spectrum without an embedded group, distorted.

Figure 37 offers a comparison of wave group 42 and wave group 44. The composition of each group is the same. However, the scaling of the seaway in which the group is embedded is different. Figure 37 demonstrates there is little effect of scaling the seaway on the kinematics of the wave group.
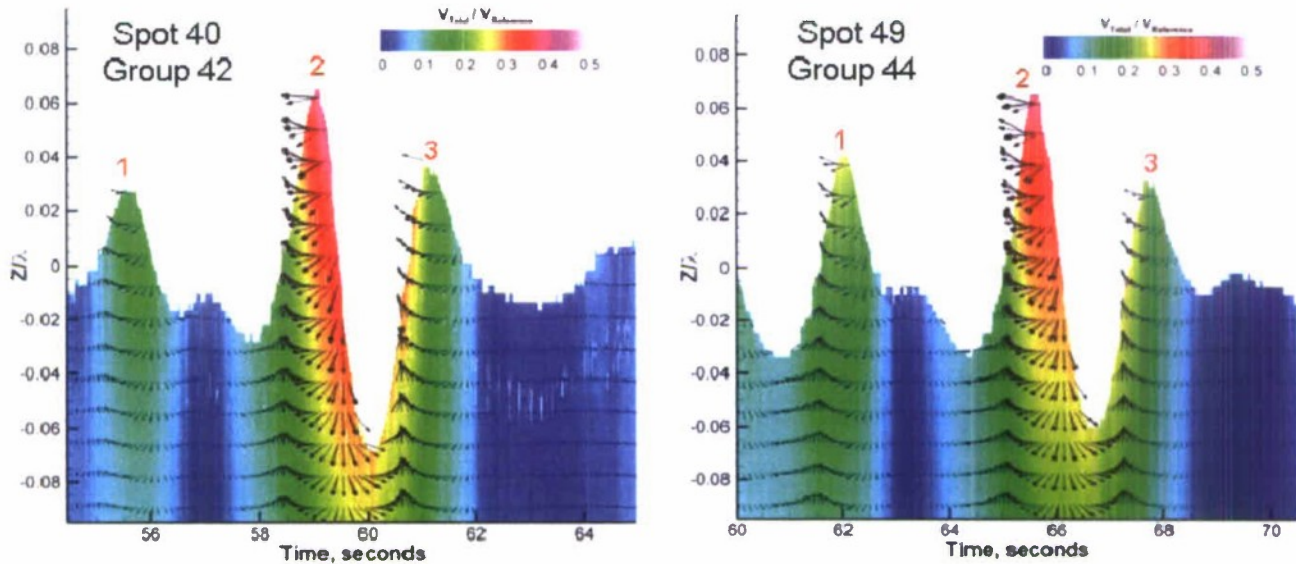
Figure 37. Velocity contour plots with total velocity vectors for wave group 42 and wave group 44.

Bretschneider Sea State 8

Figure 38 contains two plots of BS-SS8 realizations as recorded by wave probe 3, each with a different embedded wave group. The first plot in the figure contains wave group 37 and the second plot, wave group 38. The wave groups are traced in red and occur at different locations within the realization. Regardless of location, the compositions of the wave groups are similar, consisting of three waves, the second of which has the largest crest and trough.

Figure 38 shows the time history of the realization at wave probe 3. Figure 39 and Figure 40 show the velocity contour plots of each wave group, providing a bit of the wave train before and after the wave group. As discussed previously, the x-axis is compressed relative to the y-axis for visualization purposes and therefore, the relative steepness among waves has been distorted. A visual comparison shows that although the groups occur at different locations within the realization there is little difference between the resulting kinematics of the wave groups. Just as scaling of the seaway in which the group is embedded had little effect on the wave group, neither does location. It can be concluded that for the wave group generation method used in the MASK basin, the location within a realization does not affect the kinematics of the group.
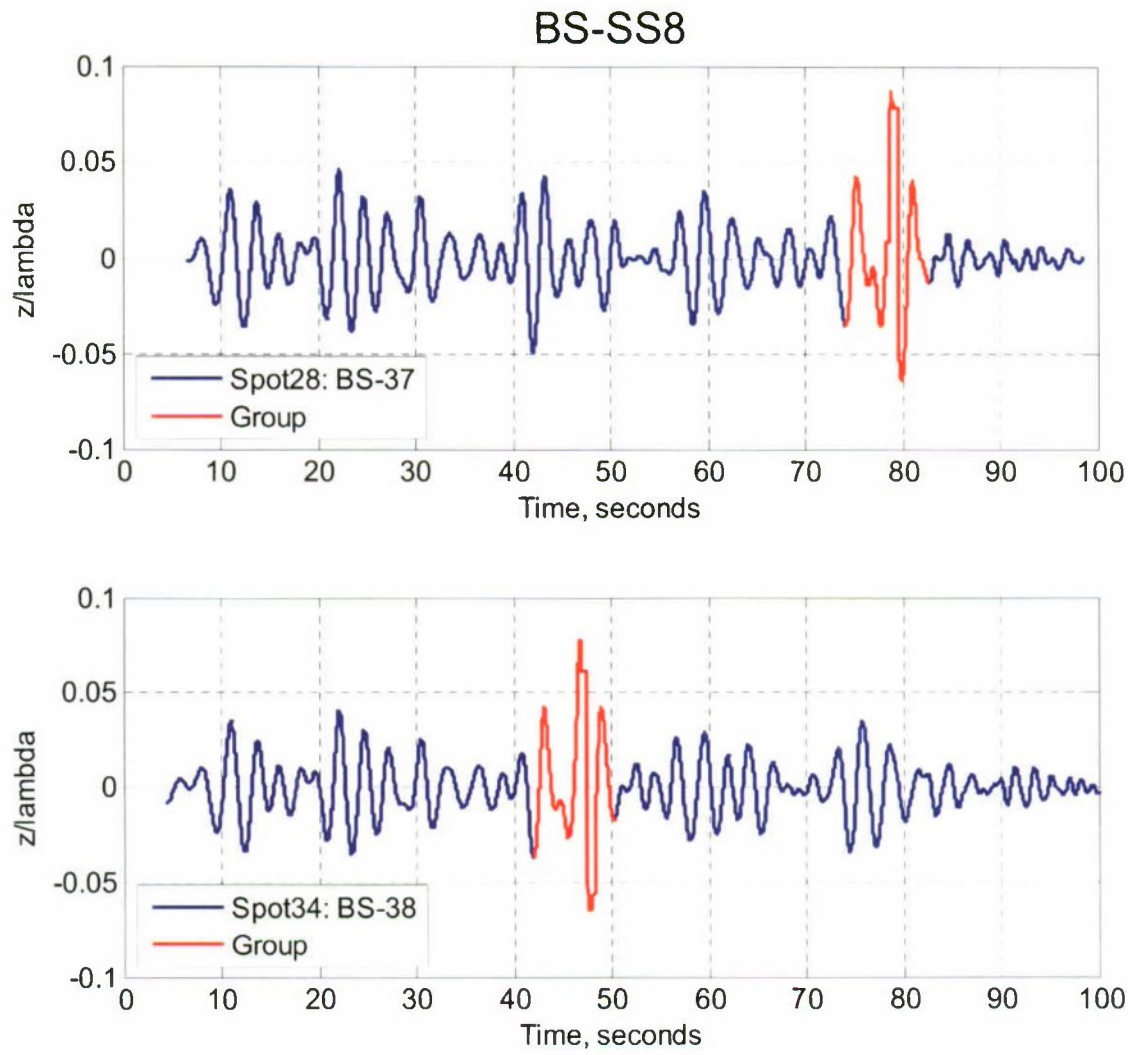
Figure 38. BS-SS8 realizations with embedded wave groups. The red tracing indicates a wave group.
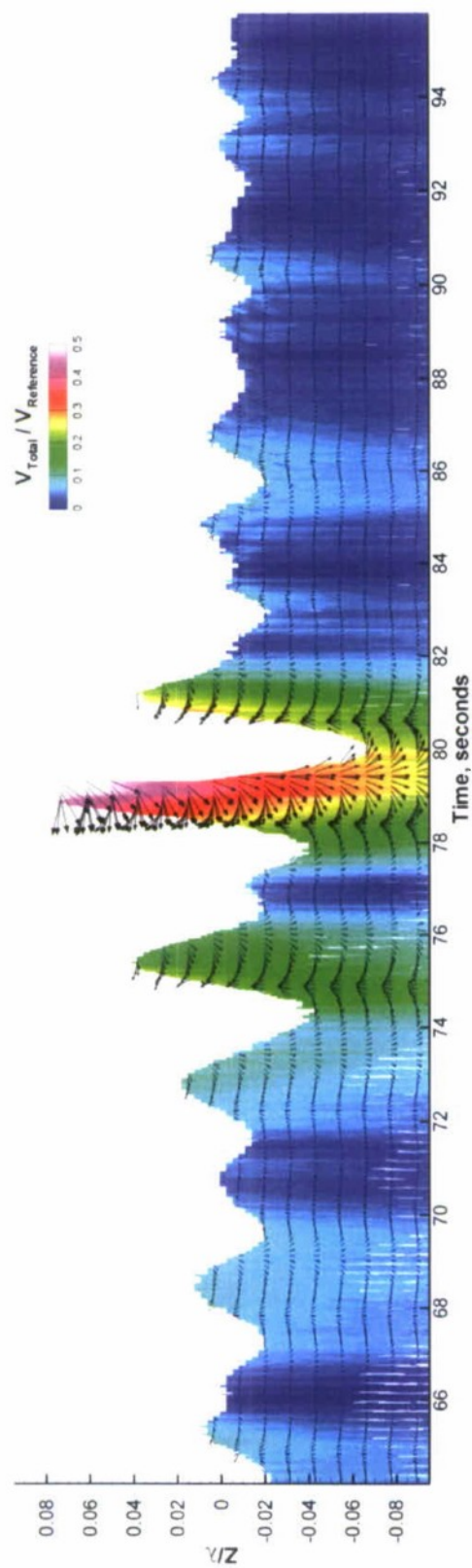
Figure 39. Velocity contour plot with total velocity vectors for wave group 37 embedded in a BS-SS8 spectrum.
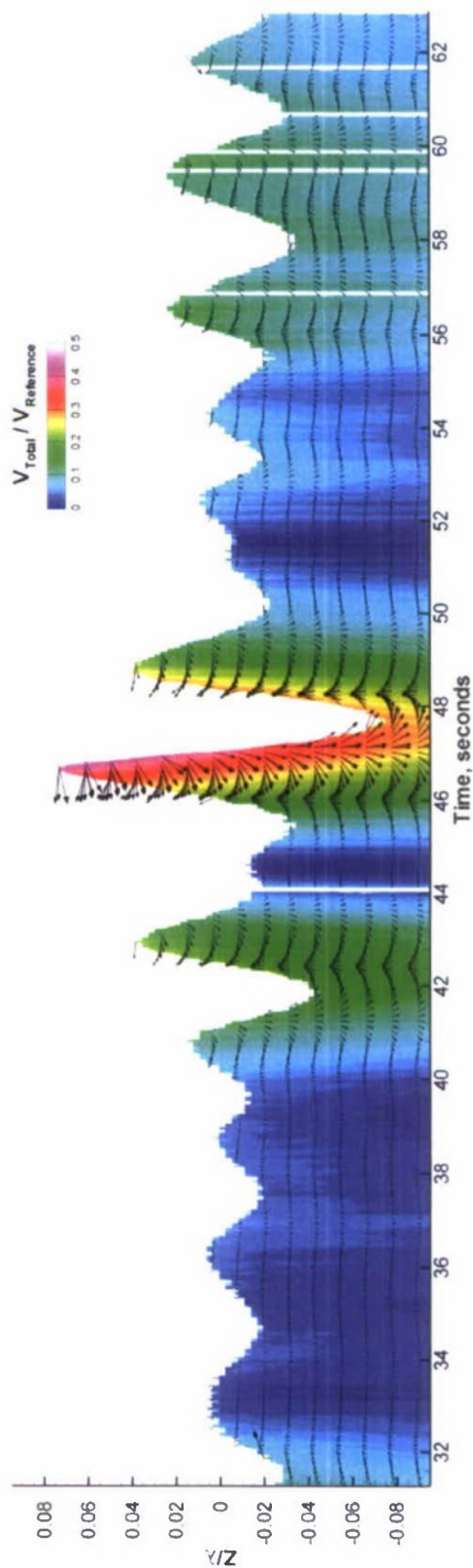

Figure 40. Velocity contour plot with total velocity vectors for wave group 38 embedded in a BS-SS8 spectrum.

This page intentionally left blank

CONCLUSIONS AND RECOMMENDATIONS

Overall, it was the intent of this experiment to collect and present a data set of the velocity field beneath the free surface of experimentally generated waves. The results from this investigation are intended to aid in the understanding of wave kinematics for experimental regular and irregular waves, specifically the kinematics of embedded wave groups within irregular waves. In addition, the results of this experiment are intended to offer a foundation to a deterministic, and hopefully more effective, approach to ship performance evaluation methods for severe conditions, which are traditionally accomplished by the use of statistical methods (for additional discussion see Bassler, et al., 2010; 2010a; Belenky, et al., 2010).

Overall, as predicted by theory, the regular wave velocity profiles followed an exponential trend, and the magnitude of the velocity increased with increasing wave steepness. While the experimental measurements exhibited the same exponential decay as theory predicted; as wave steepness increased, the velocity profiles began to deviate from theory. This deviation was most apparent in the 1/15 wave steepness condition, which is likely due to the manifestation of nonlinearities in the experimentally generated wave-field.

Both the velocity profiles and contour plots showed that the velocity field beneath regular waves is dependent on depth, but has little dependence on the position or phase of the wave. For the irregular waves and the embedded wave groups, as expected, the kinematics of the irregular waves was shown to be dependent on wave phase. In addition, the velocity contours for all of the embedded wave groups were asymmetric and chaotic, compared to relatively evenly distributed contours of the regular waves.

The kinematics of the embedded wave groups, in an irregular seaway, showed a "U-shaped" region of highest velocity between the peaks of the second and third waves of the group. This shape is most likely the result of the wave generation method used in the experiment, which uses finite length sine wave superposition, where slower waves are overtaken by faster ones as the group is formed and then dispersed. A comparison of an indigenous wave group occurring in an irregular seaway with the generated wave groups indicates the wave generation method does not significantly influence the resulting wave kinematics. If this velocity field is similar in structure to full-scale ocean wave groups, this may contribute to the severity of the response for a ship encountering the wave-field. An improved understanding of the kinematics for these large-amplitude wave groups is important to the modeling of these wave conditions in numerical codes, particularly for the assessment of ship performance.

The effects of wave group location, composition, and scaling on the wave group kinematics were also examined. It was shown, using the specified wave group generation method, the location of the wave group within the irregular seaway and the scaling of the seaway did not have a significant effect on the overall kinematics of the group. However, wave group composition was shown to have a significant effect on the kinematics. This suggests the waves which exist prior to the group do not significantly affect the kinematic properties of the group enabling additional flexibility for the evaluation of ship performance in severe wave conditions. The generated deterministic wave groups can be embedded in a variety of seaways without significantly affecting the embedded group

kinematics. The seaway before a wave group will have an influence on the initial conditions of the ship, affecting its attitude and orientation for when it encounters a wave group. However, the velocities, and therefore resulting pressures and forces acting on the ship for the most severe conditions in a seaway, will be a function of the wave group, and not the seaway in which the group is embedded, or occurred. Conversely, from the experimental observations, the composition of the wave group does influence the group kinematics, illustrating the importance of choosing appropriate group compositions to meet the ship performance evaluation objectives, whether experimentally or numerically.

It is the recommendation of the authors that a statistical approach to modeling a seaway still be completed first, to gain an initial understanding of the composition and probability of occurrence for specific rare and extreme wave events. With this knowledge, appropriate wave groups can be generated, either numerically or in the basin, to offer a deterministic solution to assessing and analyzing the dynamic stability and structural loads performance for a ship encountering such wave events. The authors hope this data set will aid in the development and improvement of numerical tools which rely on accurate modeling of wave-field kinematics to assess ship performance.

Further development to the work presented in this report, includes the use of new, enhanced wave-maker capabilities in the MASK basin (Hayden, et al., 2010), which will enable deterministic realizations of irregular seaways, including large-amplitude wave groups to be generated more easily. Additionally, for short-crested, multi-directional, irregular wave conditions, which have been a subject of interest at NSWCCD for most of the past decade, it may be possible to used advanced PIV techniques to obtain 3-D spatial wave-field kinematics measurements at selected locations in the basin. This type of investigation will further provide improved understanding of the effects of spreading and directionality on the wave-kinematics, identifying necessary considerations for modeling, and provide additional validation data for the development of advanced numerical simulation tools.

REFERENCES

AIAA (1998), *Guide for the Verification and Validation of Computational Fluid Dynamics Simulations*, American Institute of Aeronautics and Astronautics, Reston, VA, G-077-1998.

Alford, L. K., A. W. Troesch, and L. S. McCue (2006), "Design Wave Elevations Leading to Extreme Roll Motion," *Marine Systems and Ocean Technology*, 1(4), June.

Alford, L. K., M. S. Khalid, D. Kim, K. Maki, and A. W. Troesch (2007), "A Methodology for Creating Design Ship Responses," *10th Intl. Symp. on Practical Design of Ships and Other Floating Structures*, Houston, TX, 1-5 October.

Alford, L. K. (2008), Estimating Extreme Responses Using A Non-Uniform Phase Distribution, *Ph.D. Dissertation*, The University of Michigan.

Anato, E. M. and C. Guedes Soares (2008), "On the Occurrence of Abnormal Waves in an Offshore Tank," *Journal of Offshore Mechanics and Arctic Engineering*, 130, May.

Bassler, C. C., G. E. Lang, S. S. Lee, J. B. Carneal, J. T. Park, and M. J. Dipper (2008), "Formation of Large-Amplitude Wave Groups in an Experimental Model Basin," NSWCCD-50-TR-2008/025, August.

Bassler, C. C., M. J. Dipper, and G. E. Lang (2009), "Formation of Large-Amplitude Wave Groups in an Experimental Model Basin," *Proc. of the 10th Intl. Conf. on Stability of Ships and Ocean Vehicles (STAB 2009)*, St. Petersburg, Russia, 22-26 June

Bassler, C. C, V. Belenky, and M. J. Dipper (2010), "Characteristics of Wave Groups for the Evaluation of Ship Response in Irregular Seas," *Proc. 29th Intl. Conf. on Ocean, Offshore, and Arctic Engineering*, Shanghai, China, 6-11 June.

Bassler, C. C, V. Belenky, and M. J. Dipper (2010a), "Application of Wave Groups to Assess Ship Response in Irregular Seas," *Proc. 11th Intl. Ship Stability Workshop*, Wagengenin, The Netherlands, June.

Belenky, V., J. O. de Kat, and N. Umeda (2008), "Toward Performance-Based Criteria for Intact Stability," *Marine Technology* 45(2), April.

Belenky, V. C. Bassler, M. Dipper, B. Campbell, K. Weems, and K. Spyrou (2010), "Direct Assessment Methods for Nonlinear Ship Response in Severe Seas," *Proc. ITTC Workshop on Seakeeping*, Seoul, Korea, 19-21 Oct.

Blocki, W. (1980), "Ship Safety In Connection with Parametric Resonance of the Roll," *Intl. Shipbuilding Progress*, 27(306), pp.36-53.

Bishop, R.C., W. Belknap, C. Turner, B. Simon and J.H. Kim (2005), "Parametric Investigation on the Influence of GM, Roll Damping, and Above-Water Form on the Roll Response of Model 5613," Hydromechanics Dept. Technical Report, NSWCCD-50-TR-2005/027, 2005.

Bitner-Gregersen, E. M. and O. Hagen (2004), "Freak Wave Events Within the Second Order Wave Model," *Proc. of the 23rd Intl. Conf. on Offshore Mechanics and Arctic Engineering*, Vancouver, Canada, June.

Boukhanovsky, A. V. and A. B. Degtyarev (1996), "Nonlinear Stochastic Ship Motion Stability in Different Wave Regime," *Proc. 3rd Intl. Conf. in Commemoration of the 300th Anniversary of Creating Russian Fleet by Peter the Great (CRF'96)*, St. Petersburg, Russi,.

Broad, W. J. (2006), "Rogue Giants at Sea," The New York Times, July 11.

Buckley, W. H. (1983), "A Study of Extreme Waves and Their Effects on Ship Structure," Ship Structure Committee Report, SSC-320.

Buckley, W. H. (2005), "Extreme Waves for Ship and Offshore Platform Design," *SNAME Technical and Research Report No. 57,*

Carroll, R. J., C. H. Spiegelman,, and J. Sacks (1988), "A Quick and Easy Multiple-Use Calibration-Curve Procedure," *Technometrics*, 30(2), pp. 137-141.

Choi, H. (2005), "Kinematics Measurements of Regular, Irregular, and Rogue Waves by PIV/LDV," *Ph.D. Dissertation,* Texas A&M University.

Clauss, G. F. and J. Bergmann (1986), "Gaussian Wave Packets- A New Approach to Seakeeping Tests of Ocean Structures," *Applied Ocean Research*, 8(4).

Clauss, G. F. and W. L. Kuchnlein (1994), "Seakeeping Tests of Marine Structures with Deterministic Wave Groups and Tank Side Wall Wave Absorbers," *Proc. 7th Intl. Conf. on the Behavior of Offshore Structures*, Boston, MA, 12-15 July.

Clauss, G. F. and W. L. Kuehnlein (1995), "A New Approach to Seakeeping Tests of Self-Propelled Models in Oblique Waves with Transient Wave Packets," *Proc. 14th Intl. Conf. on Offshore Mechanics and Arctic Engineering*, Copenhagen, Denmark, June.

Clauss, G. F. (1999), "Task-Related Wave Groups for Seakeeping Tests or Simulation of Design Storm Waves," *Applied Ocean Research*, 21(5), October.

Clauss, G. F. (2000) "Tailor-Made Transient Wave Groups for Capsizing Tests," *Proc. 7th Intl. Conf. on Stability and Seakeeping of Ships and Ocean Vehicles (STAB 2000)*, Launceston, Australia, 7-12 February.

Clauss, G. F. (2002), "Dramas of the Sea: Episodic Waves and Their Impact on Offshore Structures," *Applied Ocean Research*, 24(3), June.

Clauss, G. F. and J. Hennig (2002), "Computer Controlled Capsizing Tests Using Tailored Wave Sequences," *Proc. 21st International Conference on Offshore Mechanics and Arctic Engineering*, Oslo, Norway, 23-28 June.

Clauss, G. F. (2002a), "Task-Related Rogue Waves Embedded in Extreme Seas," *Proc. 21st International Conference on Offshore Mechanics and Arctic Engineering*, Oslo, Norway, 23-28 June.

Clauss, G. F. (2002b), "Dramas of the Sea: Episodic Waves and Their Impact on Offshore Structures," *Applied Ocean Research*, 24(3), June.

Clauss, G. F. and J. Hennig (2004), "Deterministic Analysis of Extreme Roll Motions and Subsequent Evaluation of Capsizing Risk," *Intl. Shipbuilding Progress*, 51(2/3).

Clauss, G. F. and C.E. Schmittner (2005), "Experimental Optimization of Extreme Wave Sequences for the Deterministic Analysis of Wave/Structure Interaction," *Proc. 24th Intl. Conf. on Offshore Mechanics and Arctic Engineering*, Halkidiki, Greece, 12-17 June.

Clauss, G. F., C.E. Schmittner, and R. Stuck (2005), "Numerical Wave Tank-Simulation of Extreme Waves for the Investigation of Structural Response," *Proc. 24th Intl. Conf. on Offshore Mechanics and Arctic Engineering*, Halkidiki, Greece, 12-17 June.

Clauss, G. F. (2008), "The Taming of the Shrew: Tailoring Freak Wave Sequences for Seakeeping Tests," *J. Ship Research*, 52(3).

Clauss, G. F., C.E. Schmittner, and J. Hennig (2008), "Systematically Varied Rogue Wave Sequences for the Experimental Investigation of Extreme Structure Behavior," *J. of Offshore Mechanics and Arctic Engineering*, 130, May.

Davis, M. C. and E. E. Zarnick (1964), "Testing Ship Models in Transient Waves," *Proc. 5th Symposium on Naval Hydrodynamics*, Bergen, Norway

Dean, R. G. and R. A. Dalrymple (1984), Water Wave Mechanics for Engineers and Scientists, New Jersey: World Scientific Publishing.

Fenton, J. D. (1985), "A Fifth-Order Stokes Theory for Steady Waves," *J. of Waterway, Port, Coastal and Ocean Engineering*, 111(2), March.

Fernandes, A. C., J. Hennig, M. D. Maia, Jr., H. Cozijn, and J. S. Sales, Jr. (2008), "Worst Sea-Best Sea Wave Group Spectra from Random Sea States," *Proc. 27th Intl. Conf. on Offshore Mechanics and Arctic Engineering*, Estoril, Portugal, 15-20 June.

Gersten, A. and R. J. Johnson (1969), "Notes on Ship Model Testing in Transient Waves," NSRDC Report 2960, April.

Goda, Y. (1976), "On Wave Groups," *Proc. 1st Intl. Conf. on the Behavior of Offshore Structures*, Trondheim, Norway, pp. 115-128.

Graw, K.-U. (1994), "Comparison of Wave Theories with Velocity Measurement," *Intl. Symp. on Waves- Physical and Numerical Modeling*, Vancouver, BC, Canada, August

Guedes Soares, C., N. Fonseca, and R. Pascoal (2008), "Abnormal Wave-Induced Load Effects in Ship Structures," *J. of Ship Research*, 52(1), March.

Grue, J., D. Clamond, M. Huseby, and A. Jensen (2003), "Kinematics of Extreme Waves in Deep Water," *Applied Ocean Research*, 25.

Grue, J. and A. Jensen (2006), "Experimental Velocities and Accelerations in Very Steep Wave Events in Deep Water," *European J. of Mechanics B/Fluids*, 25, pp. 554-564.

Grue, J., L. Romero, J. Kleiss, and W. K. Melville (2008), "Orbital Velocity in Spatial Ocean Wave Elevation Measurement: Nonlinear Computation and Approximation," *Proc. 27th Intl. Conf. on Offshore Mechanics and Arctic Engineering*, Estoril, Portugal, 15-20 June.

Hayden, D., J. Hoyt, M. Melendez, H. Moeller, Y. Bargman, S. Carpenter, S. Turner (2010), "Naval Surface Warfare Center's Wavemaker Modernization Program," *Proc. 29th American Towing Tank Conference*, Annapolis, MD, 11-13 August.

Hennig, J., H. Billerbeek, G. F. Clauss, D. Testa, K. E. Brink, and W. L. Kuhnlein (2006), "Quantitative and Qualitative Validation of a Numerical Code for the Realistic Simulation of Various Ship Motion Scenarios," *Proc. 25th Intl. Conf. on Offshore Mechanics and Arctic Engineering*, Hamburg, Germany, 4-9 June.

Jensen, A., J. Sveen, J. Grue, J.-B. Richon, C.Gray, (2001) "Accelerations in water waves by extended particle image veloeimetry," *Experiments in Fluids*, 30, pp. 500-510.

Jensen, A. and G. Pedersen, (2004) "Optimization of acceleration measurements using PIV," *Measurement Science and Technology*, 15, pp. 2275-2283.

Kristiansen, T., R. Baarholm, G. Rortiveit, E. Hansen, and C. Stansberg (2005), "Kinematics in a Diffracted Wave Field: Particle Image Velocimetry (PIV) And Numerical Models," *Proc. 24th Intl. Conf. on Ocean, Offshore, and Arctic Engineering*, Halkidiki, Greece, 12-17 June.

Longuet-Higgins, M. S. (1976), "On the Nonlinear Transfer of Energy in the Peak of a Gravity-Wave Spectrum: A Simplified Model," *Proc. Royal Society of London A*, 347, pp.311-328.

Longuet-Higgins, M. S. (2008), "On an Approximation to the Limiting Stokes Wave in Deep Water," *Wave Motion*, 45(6), pp. 770-775.

Masterton, S. R. and C. Swan (2008), "On the Accurate and Efficient Calibration of a 3D Wave Basin," *Ocean Engineering*, 35(8-9), June.

Matos, V., J. S. Sales Jr., and S. H. Sphaier (2005), "Seakeeping Tests with Gaussian Wave Packets," *24th International Conference on Offshore Mechanics and Artic Engineering*, Halkidiki, Greece, 12-17 June.

Minnick, L., C. Bassler, S. Percival, and L. Hanyok (2010), "Large-Scale Wave Kinematics Measurements of Regular Waves and Large-Amplitude Wave Groups," *Proc. 29th Intl. Conf. on Ocean, Offshore, and Arctic Engineering*, Shanghai, China, 6-11 June.

National Transportation Safety Board (2005), NTSB Marine Accident Brief: Heavy-Weather Damage to Bahamas-Flag Passenger Vessel Norwegian Dawn, NTSB/MAB-05/03, 16 April.

Ning, D. Z., B. Teng, R. E. Eatock Taylor, and J. Zang (2008), "Numerical Simulation of Non-Linear Regular and Focused Waves in an Infinite Water-Depth," *Ocean Engineering*, 35(8-9), June.

O'Dea, J.F. and J. N. Newman (2007), "Numerical Studies of Directional Wavemaker Performance," *Proc. 28th American Towing Tank Conf.*, Ann Arbor, MI, 9-10 August.

Onorato, M., A. R. Osborne, and M. Serio (2006), "Modulational Instability in the Crossing Sea States: A Possible Mechanism for the Formation of Freak Waves," *Physical Review Letters*, 96.

Philips, O. (1994), "The Structure of Extreme Ocean Waves," *Proc. 20th Symp. on Naval Hydrodynamics*, Santa Barbara, California, 21-26 August.

Ross, S. M. (2004), *Introduction to Probability and Statistics for Engineers and Scientists*, Third Edition, Amsterdam: Elsevier, Academic Press.

Scheffe, H. (1973), "A Statistical Theory of Calibration," *The Annals of Statistics*, 1(1), pp. 1-37.

Schumann, E. H. (1980), "Giant Wave," *Oceans*, July, pp. 27-30.

Sclavounos, P. D. (2005), "Nonlinear Particle Kinematics of Ocean Waves," *J. of Fluid Mechanics*, 540, pp. 133-142.

Schmittner, C., S. Kosleck, and J. Hennig, (2010), "Predication of Wave Crest and Height Distributions and Wave Groups Using a Numerical Wave Tank," *Proc. 29th Intl. Conf. on Ocean, Offshore, and Arctic Engineering*, Shanghai, China, 6-11 June.

Skjelbreia, J., A. Torum, E. Berek, O.T. Gudmestad, J. Heidman, N. Spidsoe. (1989) "Laboratory Measurements of Regular and Irregular Wave Kinematics," *E&P Forum Workshop on Wave and Current Kinematics and Loading*, Rueil Malmaison, France, 25-26 October.

Skjelbreia, J., G. Berek, Z. Bolen, O.T. Gudmestad, J. Heidman, R. Ohmark, N. Spidsoe A. Torum,. (1991) "Wave Kinematics in Irregular Waves," *Proc. 10th Intl. Conf. on Ocean, Offshore, and Arctic Engineering*, Stavanger, Norway, 23-28 June.

Smith, C. B. (2006), Extreme Waves, Washington, DC: Joseph Henry Press.

Smith, T.C., L. K. Hanyok, and M.J. Hughes (2007), "MASK Waves Benchmark," NSWCCD-50-TR-2007/052, October.

Spyrou, K. J. (2004), "Criteria for Parametric Rolling?," *Proc. 7th Intl. Ship Stability Workshop*, Shanghai, China, 1-3 November.

Stansberg, C. T. and O. T. Gudmestad (1996), "Nonlinear Random Wave Kinematics Models Verified Against Measurements in Steep Waves," *Proc. 15th Intl. Conf. Offshore Mechanics and Arctic Engineering*, Florence, Italy, 16-20 June.

Stansberg, C. T., O. T. Gudmestad, and S. K. Haver (2008), "Kinematics Under Extreme Waves," *J. of Offshore Mechanics and Arctic Engineering*, 130, May.

Stokes, G. G. (1847), "On the Theory of Oscillatory Waves," *Trans. Cambridge Philosophic Society*, 8, pp.441-455

Su, M.-Y., M. Bergin, and S. Bales (1982), "Characteristics of Wave Groups in Storm Seas," *Proc. Ocean Structural Dynamics Symp. '82*, Corvallis, Oregon, pp. 118-132.

Su, M.-Y. (1986), "Large, Steep Waves, Wave Grouping and Breaking," *Proc. 16th Symp. on Naval Hydrodynamics*, Berkeley, California, July.

Swan, C., T. Bashir, and O. T. Gudmestad (2002), "Nonlinear Inertial Loading. Part 1: Accelerations in Steep 2-D Water Waves, *J. Fluids and Structures*, 16, pp. 391-416.

Takezawa, S. and M. Takekawa (1976), "Advanced Experiment Technique for Testing Ship Models in Transient Water Waves, Part I: The Transient Test Technique on Ship Motions in Waves," *Proc. 11th Symp. on Naval Hydrodynamics*, University College, London.

Takezawa, S. and T. Hirayama (1976), "Advanced Experiment Technique for Testing Ship Models in Transient Water Waves, Part II: The Controlled Transient Water Waves

for Using in Ship Motion Tests," *Proc 11th Symp. on Naval Hydrodynamics*, University College, London.

Themelis, N. and K. J. Spyrou (2007), "Probabilistic Assessment of Ship Stability," *SNAME Maritime Technology Conf. & Expo and Ship Production Symposium*, Fort Lauderdale, FL, November 14-16.

Themelis, N. and K. J. Spyrou (2008), "Probabilistic Assessment of Ship Stability Based on the Concept of Critical Wave Groups," *Proc. 10th Intl. Ship Stability Workshop*, Daejeon, Korea, 23-25 March.

Tikka, K. K. and J. R. Paulling (1990), "Predictions of Critical Wave Conditions for Extreme Vessel Response in Random Seas," *4th Intl. Conf. on the Stability of Ships and Ocean Vehicles (STAB '90)*, Naples, Italy.

Toffoli, A., J. M. Lefevre, J. Monbaliu, and E. Bitner-Gregersen (2004), "Dangerous Sea-States for Marine Operations," *Proc. 14th Intl. Offshore and Polar Engineering Conf.*, Toulon, France, 23-28 May.

Wheeler, J.D. (1969), "Method of Calculating Forces Induced by Irregular Waves," *Proc. of the First Offshore Technology Conf. (OTC)*, Houston, TX, 1:71-82.

Yu, Y.-X. and S.-X. Liu (1990), "The Group Characteristics of Sea Waves," *Proc. 22nd Intl. Conf. on Coastal Engineering*, Delft, The Netherlands, 2-6 July.

APPENDIX A: REGULAR WAVE TIME HISTORIES
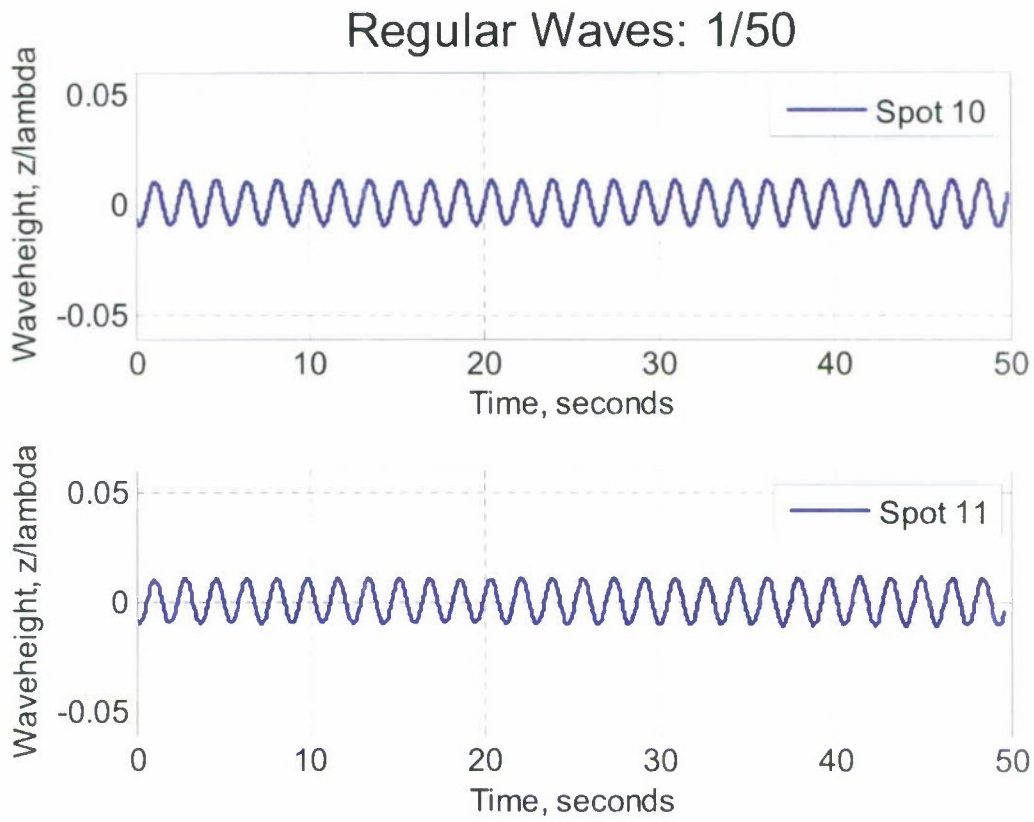
## Regular Waves: 1/50

Figure A1. Time histories for 1/50 wave steepness.
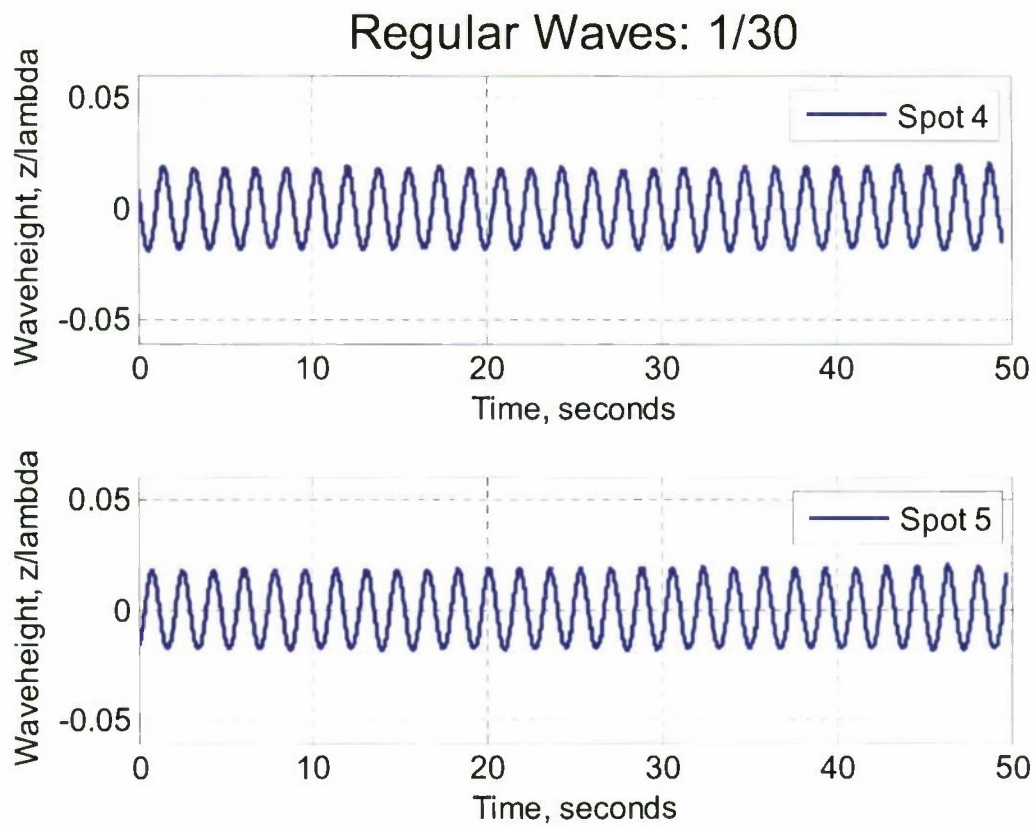
Figure A2. Time histories for 1/30 wave steepness.
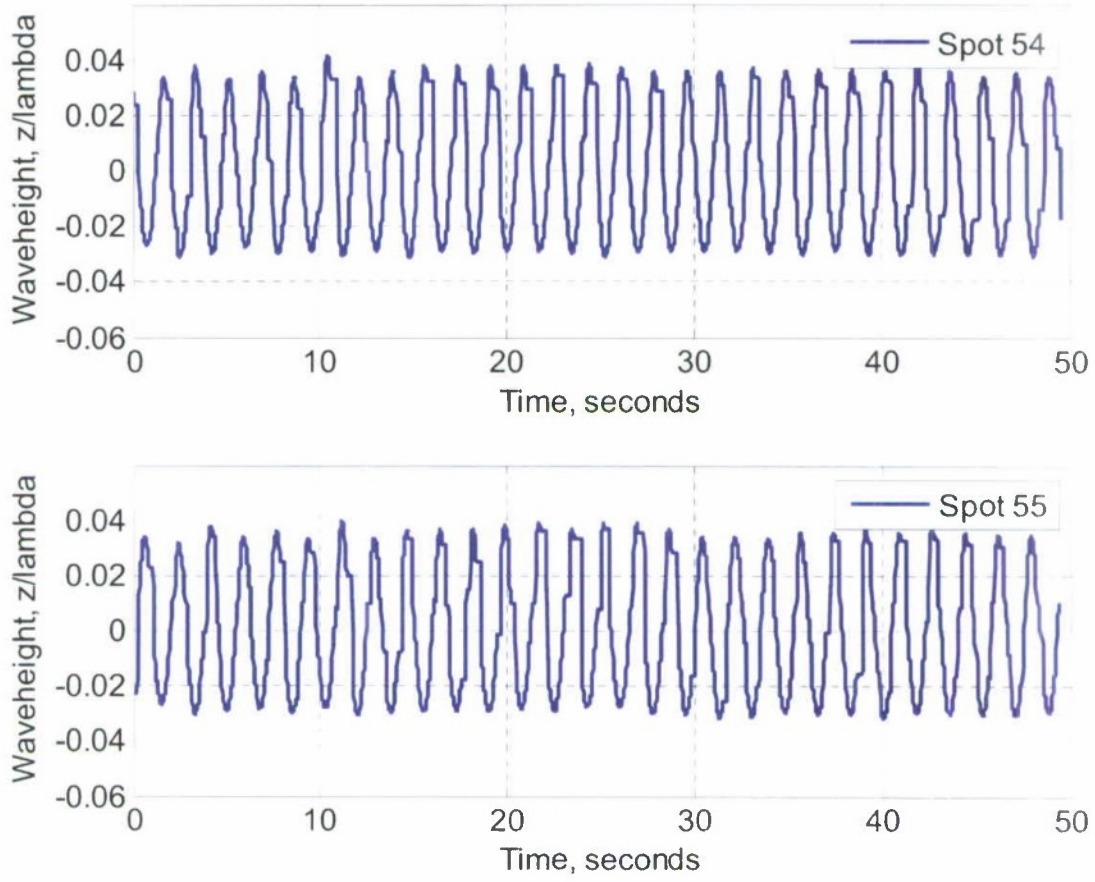
Figure A3. Time histories for 1/15 wave steepness.

This page intentionally left blank.

APPENDIX B: WAVE THEORY

Linear Wave Theory

Linear wave theory assumes a 2-D inviscid, irrotational, constant density flow. To satisfy linear approximations of the boundary conditions it also assumes periodic waves of relatively small amplitude. Using linear wave theory, the velocity components for a particle at a given depth relative to the calm water free surface, $z=0$, in a wave can be determined using (B-1) and (B-2).

$$v_x = \eta_o \frac{g}{c} \frac{\cosh[k(z+h)]}{\cosh(kh)} \cos\theta \qquad (B-1)$$

$$v_z = \eta_o \frac{g}{c} \frac{\sinh[k(z+h)]}{\cosh(kh)} \sin\theta \qquad (B-2)$$

The derivation can be found in standard textbooks (such as Dean and Dalrymple, 1984). Applying the deep water approximation (depth $> \lambda/2$), which assumes $kh \rightarrow \infty$, (B-1) and (B-2) can be reduced to:

$$v_x \approx \eta_o k \sqrt{\frac{g}{k}} e^{kz} \cos\theta \qquad (B-3)$$

$$v_z \approx \eta_o k \sqrt{\frac{g}{k}} e^{kz} \sin\theta \qquad (B-4)$$

As shown in (B-3) and (B-4), the velocity of a particle is dependent on its depth relative to the calm water reference, z, and the phase of the wave, θ. The magnitude of the total velocity, V_{Total}, at a given depth can be determined from the individual velocity components. For a given depth below the free surface, taking $\eta_o k \sqrt{\frac{g}{k}} e^{kz}$ as a constant, C_1, the total velocity is:

$$V_{Total} = \sqrt{v_x^2 + v_z^2} = \sqrt{C_1^2(\sin^2\theta + \cos^2\theta)} = C_1 \qquad (B-5)$$

Equation B-5 shows that linear wave theory predicts the magnitude of the velocity of a particle at a given depth below the free surface of a regular wave to be constant regardless of the phase of the wave.

Stokes 2nd Order Wave Theory

Stokes 2nd-order approximation does not assume the waves are infinitesimally small, but instead of finite height, eliminating some approximations made for linear theory. The free surface profile for a deep-water 2nd-order Stokes wave (Stokes, 1847) is given in (B-6).

$$\eta = \eta_o \cos(kx) + \pi \frac{A^2}{\lambda} \cos(2kx) \qquad (B-6)$$

The second order model of the particle velocity components is shown in (B-7) and (B-8).

$$v_x = \eta_o \frac{g}{c} \frac{\cosh k(h+z)}{\cosh kh} \cos\theta + \frac{3}{16} \frac{H^2 \sigma \cdot k \cosh 2k(h+z)}{\sinh^4 kh} \cos 2\theta \qquad \text{(B-7)}$$

$$v_z = \eta_o \frac{g}{c} \frac{\sinh k(h+z)}{\cosh kh} \sin\theta + \frac{3}{16} \frac{H^2 \sigma \cdot k \sinh 2k(h+z)}{\sinh^4 kh} \sin 2\theta \qquad \text{(B-8)}$$

The derivation of these equations can also be found in standard textbooks (such as Dean and Dalrymple, 1984). The presence of the 2nd-order term increases the particle velocities, which are varied along the wave due to the phase function. For example, horizontal velocities are increased at the wave crest but are reduced at the wave trough.

APPENDIX C: IRREGULAR WAVE TIME HISTORIES

Hurricane Camille
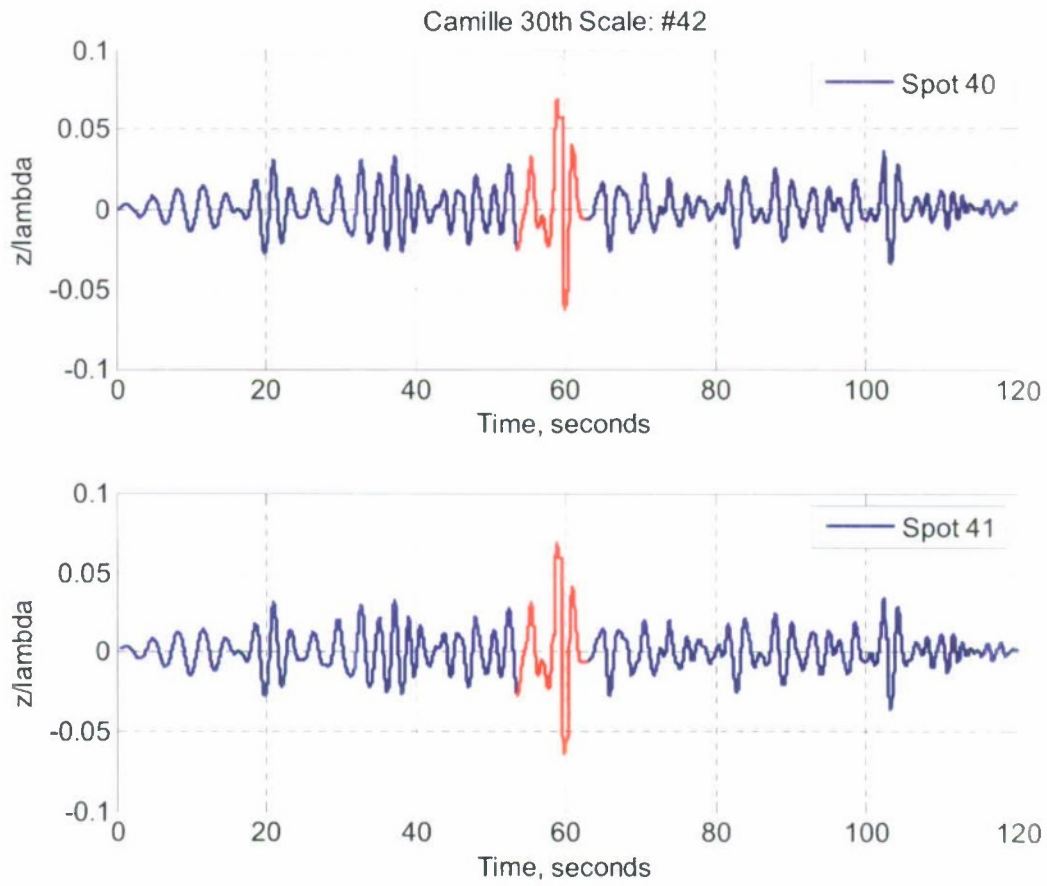
Figure C1. Hurricane Camille, 30th Scale, wave group 42.
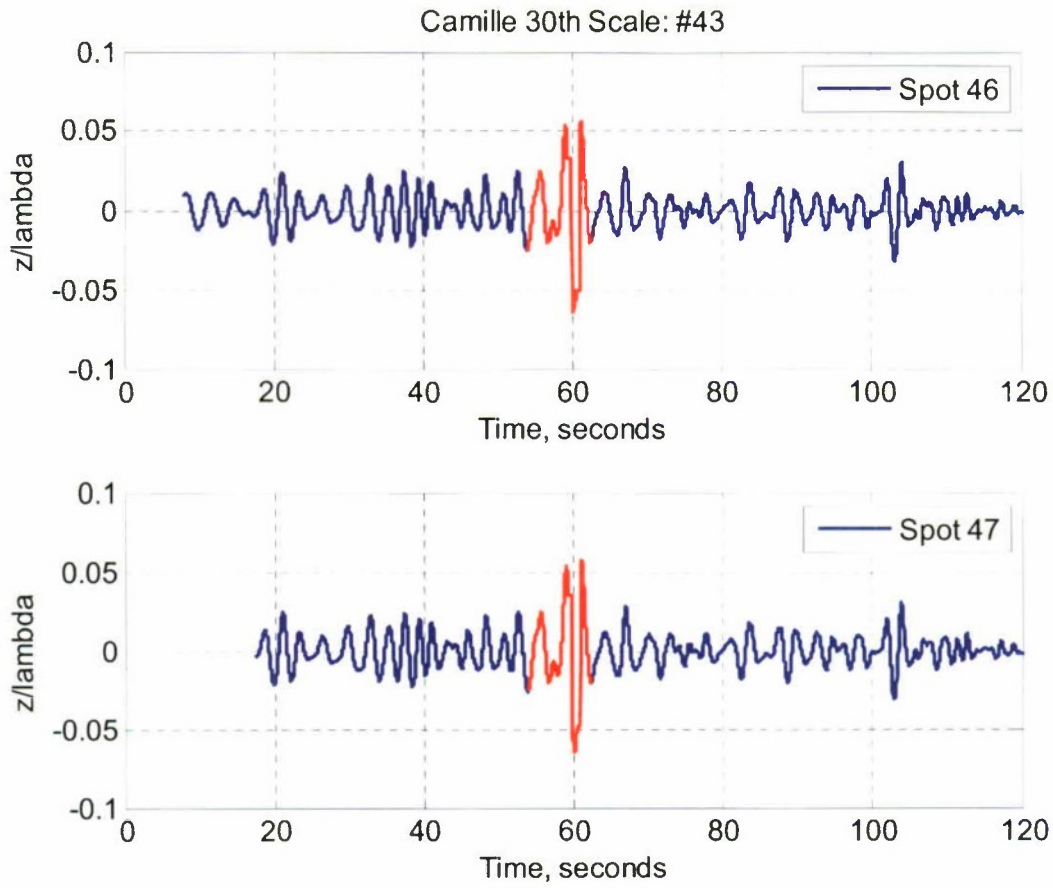
Figure C2. Hurricane Camille, 30th Scale, wave group 43.
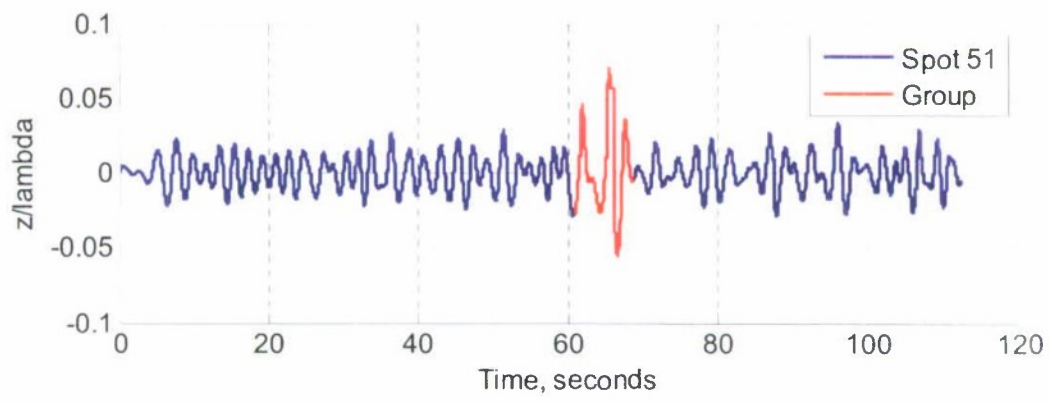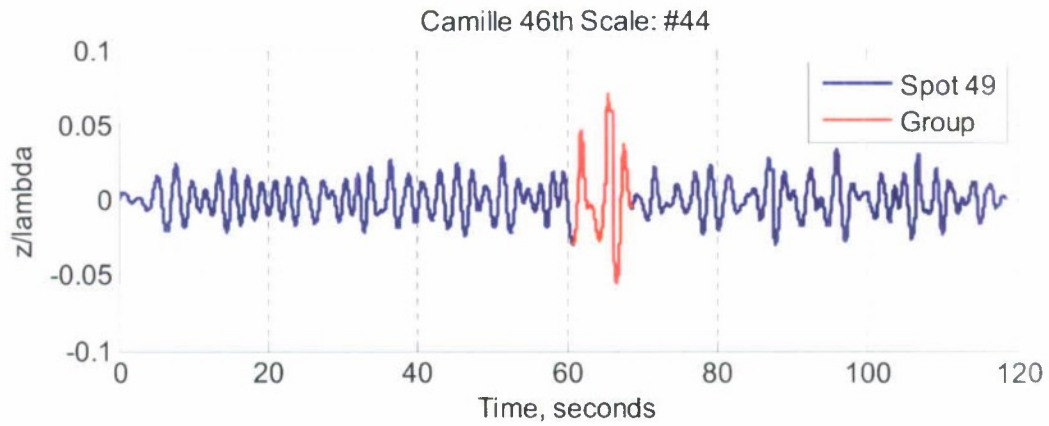
Figure C3. Hurricane Camille, 30th Scale, wave group 44.

Bretschneider Sea State 8 (BS -SS8)
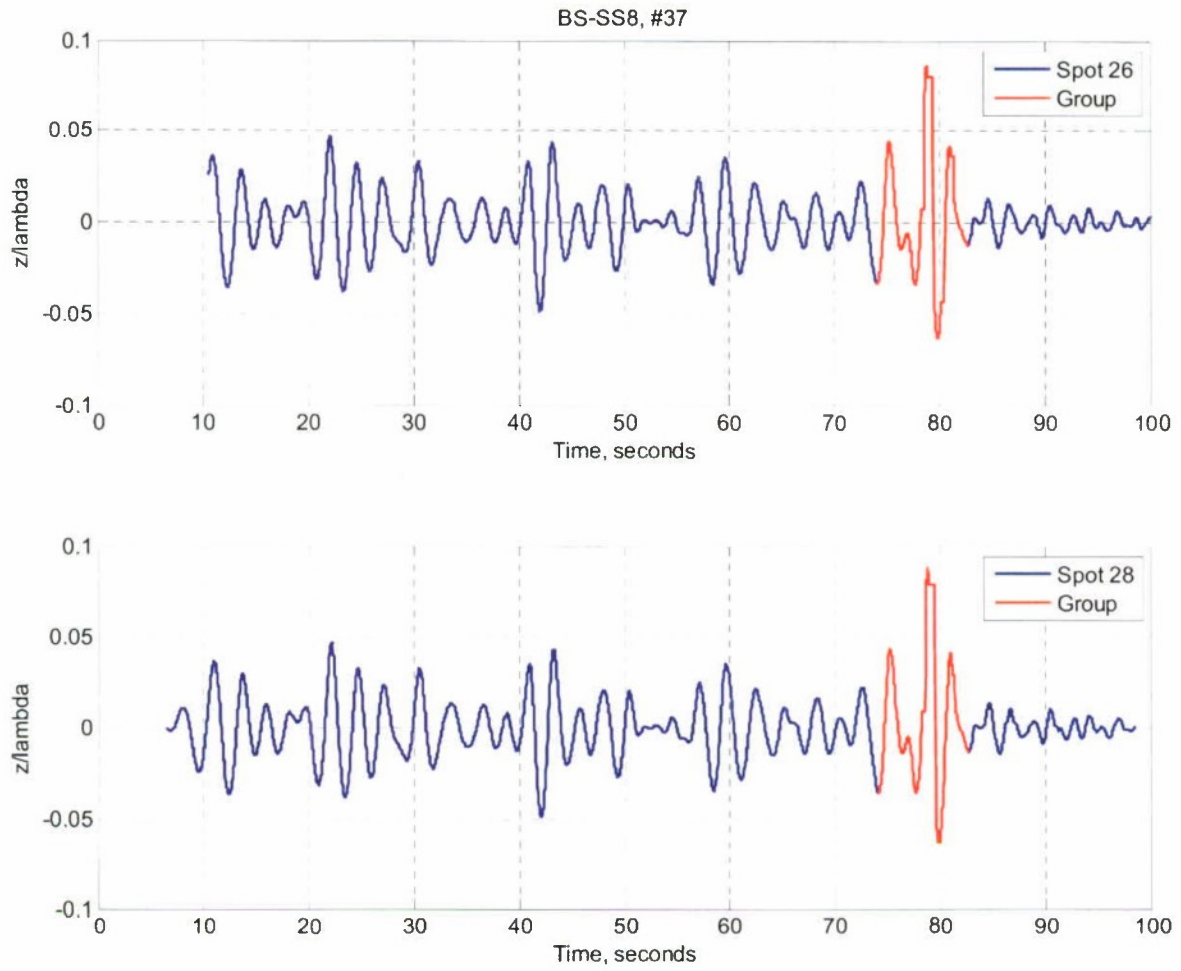
Figure C4. BS-SS8, wave group 37.
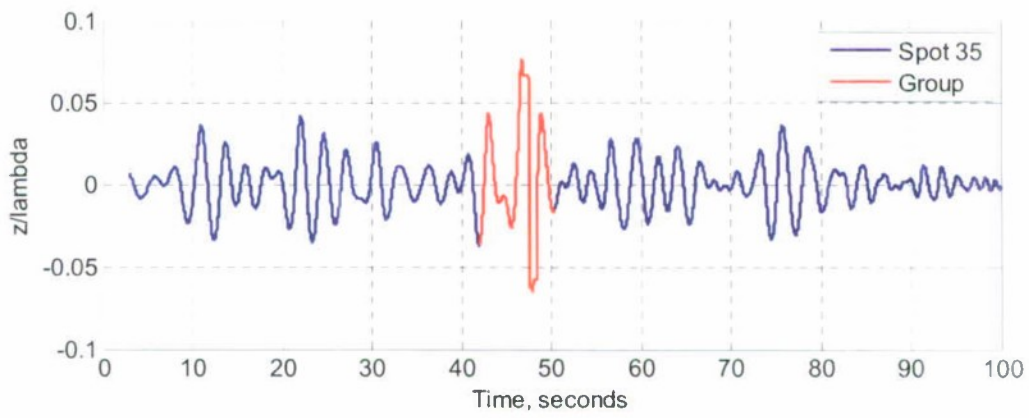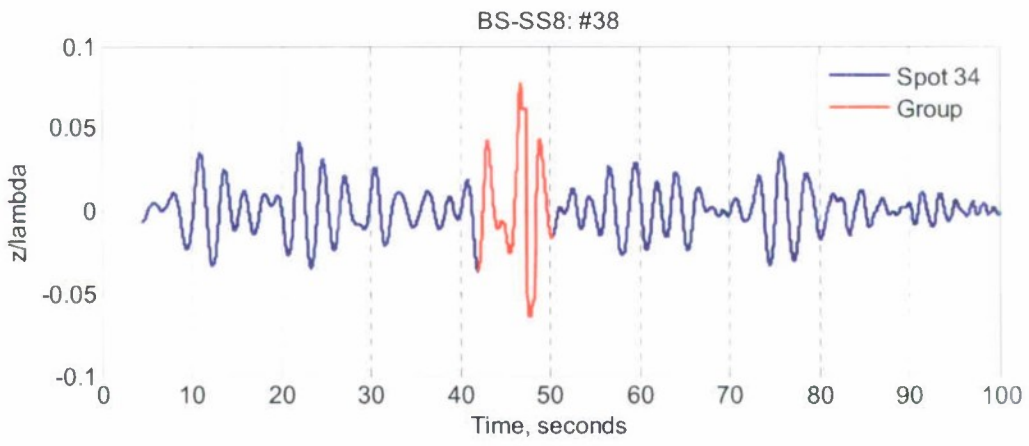
Figure C5. BS-SS8, wave group 38.

This page intentionally left blank.

Distribution List

Number of Copies	Office	Individual	Total Copies
1	NAVSEA 05D1	J. Webster	1
1	ONR 331	L. Patrick Purtell	2
1	NAVSEA 05D3	R. Dean	3
1	DTIC		4

Number of Copies	NSWCCD Code	Individual	Total Copies
1	3452 (Library)	(pdf only)	
1	0120	J. Barkyoumb	5
1	50	J. Etxegoien	6
1	504	A. Reed	7
1	505	T. Fu	8
1	506	D. Walden	9
1	5500	T. Applebee	10
1	5500	M. Dipper	11
1	5500	T. Smith	12
1	5500	J. Hickok (pdf only)	
1	5500	D. Hayden (pdf only)	
1	5500	J. Hoyt (pdf only)	
3	5500	C. Bassler	15
1	5500	S. Percival	16
1	5500	L. Hanyok	17
1	5500	V. Belenky	18
1	5500	W. Belknap (pdf only)	
1	5500	B. Campbell (pdf only)	
1	5500	T. Carrico (pdf only)	
1	5500	S. Lee (pdf only)	
1	5500	D. Wundrow (pdf only)	
3	5600	L. Minnick	21
1	5600	D. Drazen (pdf only)	
1	5600	P. Atsavapranee	22
1	5800	D. Walker (pdf only)	
1	5800	R. Hurwitz (pdf only)	

This page intentionally left blank.